SCIENCE & MILITARY

No 1 | Volume 16 | 2021

SCIENCE & MILITARY

The rationale for publishing this periodical by the Armed Forces Academy of General Milan Rastislav Štefánik is to enable the authors to publish their articles focused on particular scientific issues in the following areas: Military, Engineering, Computer Science and Technology.

Original scientific articles will be published twice a year.

Editorial Board

Published by: Armed Forces Academy of General Milan Rastislav Štefánik, Demänová 393, 031 01 Liptovský Mikuláš, Slovak Republic. IČO 37 910 337. Registered No: EV 2061/08. ISSN 1336-8885 (print). ISSN 2453-7632 (on-line).
Printed by: Armed Forces Academy of General Milan Rastislav Štefánik, Demänová 393, 031 01 Liptovský Mikuláš, Slovak Republic. Order forms should be returned to the editorial office. Published biannually.
The subscription rate for one year is 7,30 €.

The journal Science & Military is included in following multiple databases: EBSCO. ProQuest Central: PQ Science Journals; PQ Military Collection; PQ Computing; PQ Telecommunications; Illustrata: Technology; Forthcoming Technology Research Database (TRD) full text packages.

Address of the editorial office
SCIENCE & MILITARY
Armed Forces Academy of General Milan Rastislav Štefánik, Demänová 393, 031 01 Liptovský Mikuláš, Slovak Republic

Phone: +421-960-423065 Fax: +421- 044-55 222 47 E-mail: redakcia@aos.sk http://sm.aos.sk

DOI: https://doi.org/10.52651/sam.j.2021.1

SCIENCE & MILITARY

No 1 | Volume 16 | 2021

Dear Readers,

Let me talk to you for the first time as the Editor-in-Chief of the Science & Military journal. I would like to thank Assoc. Prof. Dipl. Eng. Vladimír Andrassy, PhD. for his dedication and work he has done for our journal. Assoc. Prof. Andrassy will continue working as a member of the editorial board.

Since the very beginning, the editorial board of the Science & Military journal has been pursuing its goal of publishing an attractive and high quality scientific journal focused on military science, which will be accessible to a wider public in Slovakia and abroad. We are well aware of the fact that this goal cannot be achieved overnight. Therefore, we are trying to improve the Science & Military journal all the time and this year is no exception. The journal has undergone several changes since its beginning, including the most significant change in its emphasis. Beginning with its first issue of 2021, it will be a monothematic journal focused on technical sciences (information technologies, electronics, engineering, etc.).

The editorial board has begun to use the benefits of the digital object identifier (DOI) system in order to enhance the Science & Military journal prestige. Registration of digital documents with the DOI system allows accurate identification, promotes authors' publications in the scientific world, encourages cooperation among authors of scientific writing and contributes to sharing of knowledge and expertise. In addition, the DOI system promotes academic communication and open science and enhances publication and citation ethics.

One of the long-term goals of the Science & Military editorial board is the registration of the journal with the Scopus and Current Contents databases. We will do our best to enhance its quality, scientific prestige and rankings.

Dear readers, this issue of the Science & Military journal offers interesting articles, which have undergone a rigorous peer review process. I believe they will inspire you and that they will initiate scientific discussions.

The first article written by Vladimír Popardovský, Peter Bondra and Lukáš Novotný titled ***"Proposal of Unmanned Ground Vehicle Powered by Fuel Cell"*** *deals with the design of an unmanned ground vehicle (UGV) with electric drive, using a fuel cell as a source of electricity. The UGV design, taking into account specific technical parameters, is processed into a model in the simulation environment MATLAB / Simulink / Simscape.*

The following article titled ***„Dilatometric Analysis Tool Steel X153CRMOV12"*** *written by Michal Krbaťa and Róbert Cíger presents some results of phase transformations and austenitizing behaviour of the X155CrMoV12 tool steel. Dilatation analyses of a series of samples were performed at various cooling rates, chosen in the range from 10 °C·s^{-1} to 0.1 °C·s^{-1}. Acquired experimental data were used for evaluation of dilatometric curves in order to map the temperature ranges of phase transformations of the austenite to pearlite, bainite or martensite.*

The second part of this article, titled ***"Experimental Determination of Continuous Cooling Transformation Diagram for High Strength Steel X153CRMOV12"****, deals with these analyses of the cooling curve microstructure.*

The author Maroš Eckert wrote the article titled ***"Stress Prediction Analysis during Hot Working of 100MNCRW4 STEEL"****. The aim of this paper is to analyse the possibility of using a constitutive model based on the Arrhenius equation for tool steel 100MnCrW4. Experimental measurements were performed on a DIL 805 dilatometer in the range of strain rate 0.001 s-1 for 10 s -1 and temperature from 800 to 1200 °C.*

Another article titled ***„The Role and the Risks of Explosive Ordnance Decontamination in Hungary"*** *was written by István Ember. This article analyses the work of explosive ordnance disposal specialists in Hungary and shows us the world of EOD operators. Thousands of explosive remnants of war are still waiting in the soil to be disposed of. This public duty demands highly trained professionals who are able to meet the requirements of this lethal profession.*

The series of articles is closed with the paper titled ***„Performance Characteristics of Steel 1.2842 after Nitridation"*** *written by Michal Krbaťa and Jana Escherová.. This article deals with the change in mechanical properties and wear of 1.2842 universal tool steel after plasma nitriding, which is widely used to produce cutting tools with good durability and low operating costs. The results of experiments have shown that plasma nitriding process significantly improves the mechanical and tribological properties of selected materials.*

On my behalf and on the behalf of the editorial board, I would like to thank our readers for their interest in the journal and the authors for their excellent articles, thanks to which we could publish this issue.

Brig. Gen. (ret.) Assoc. Prof. Eng.
Boris ĎURKECH, CSc.
Editor-in-Chief

Reviewers

Prof. Dipl. Eng. Viktor **FERENCEY**, PhD.	Slovak University of Technology in Bratislava, SK
Prof. Dipl. Eng. Karel **FRYDRÝŠEK**, Ph.D.	VSB - Technical University of Ostrava, CZ
LTC Dipl. Eng. Alexander **HUGYÁR**	NATO EOD Centre of Excellence, Trenčín, SK
Prof. Dipl. Eng. Pavel **KONEČNÝ**, Ph.D.	University of Defence in Brno, CZ
Assoc. Prof. Dipl. Eng. Daniel **KOTTFER**, PhD.	Technical University of Košice, SK
Assoc. Prof. Dipl. Eng. Mariana **KUFFOVÁ**, PhD.	Armed Forces Academy of General M. R. Štefánik, Liptovský Mikuláš, SK
Prof. Dipl. Eng. Jiří **STODOLA**, DrSc.	University of Defence in Brno, CZ
Assoc. Prof. Dipl. Eng. Zbyněk **STUDENÝ**, Ph.D.	University of Defence in Brno, CZ
Assoc. Prof. Dipl. Eng. Miroslav **TOMÁŠ**, PhD.	Technical University of Košice, SK

DOI: https://doi.org/10.52651/sam.a.2021.1.5-13

PROPOSAL OF UNMANNED GROUND VEHICLE POWERED BY FUEL CELL

Vladimír POPARDOVSKÝ, Peter BONDRA, Lukáš NOVOTNÝ

Abstract: The presented article deals with the design of an unmanned ground vehicle (UGV) with electric drive, using a fuel cell as a source of electricity. The introduction describes the principle of the fuel cell, followed by the design of the UGV propulsion system. The UGV design, taking into account specific technical parameters, is processed into a model in the simulation environment MATLAB / Simulink / Simscape. Simulation results are presented in graphical form of selected physical quantities over time.

Keywords: Unmanned ground vehicle; UGV; Fuel cell; MATLAB.

1 INTRODUCTION

Unmanned vehicles are widely used in the civilian and military spheres. They are used as carriers of various types of payloads. The determining parameter of their use is primarily the method of their drive. From the point of view of military use, the electric drive appears to be very promising, which has several advantages (high efficiency, high torque, quiet operation).

The problem with the electric motor, however, is the energy source - current batteries, especially based on lithium, still have a low energy density. This results in a short operating time during which such an accumulator is able to supply energy to the electric motor. The solution could be another energy carrier - e.g. hydrogen. Fuel cells are devices in which hydrogen is chemically reacted with atmospheric oxygen to produce water, heat and electricity. This paper deals with the use of a fuel cell as a source of electrical energy for an unmanned electric vehicle. The aim was to design the concept of such a vehicle.

2 FUEL CELL

A fuel cell is an electrochemical device that is capable of directly converting the chemical energy contained in a fuel into electrical energy. The result of the chemical reaction is direct current, water and waste heat.

They consist of two electrodes, between which there is a layer of electrolyte. There are two electrodes, a negative electrode - an anode and a cathode. The electrodes are coated on the surface with a layer of catalyst in the form of a precious metal, e.g. platinum or nickel. [1]

2.1 Polymer-electrolyte membrane fuel cells / proton exchange membrane (PEMs/PEFCs)

PEM fuel cells provide a high degree of energy density and their advantage is low weight and volume compared to other cells. They are the most used type of articles. They have a high energy density with respect to the area, up to 0.7 W.cm^{-2}. The membrane passes only positively charged hydrogen ions from the anode to the cathode, i.e. only in one direction. It does not let through reaction gases or electrons. The electrodes are porous and contain a platinum catalyst. Thus, only hydrogen and atmospheric oxygen are needed for them to function. [2]

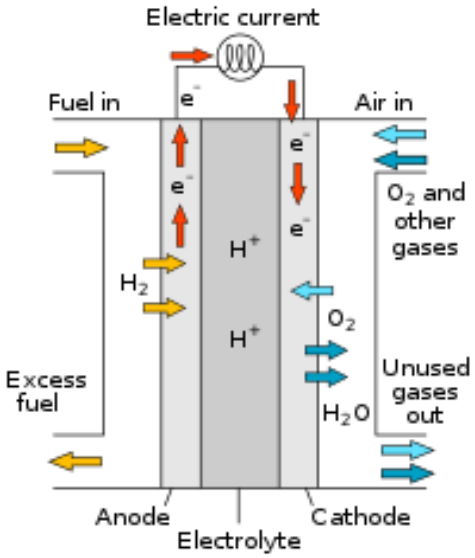

Fig. 1 Principle scheme of the fuel cell
Source: [3].

Hydrogen reacts at the anode, releasing electrons and becoming a positively charged ion. These H^+ ions travel through the electrolyte to the cathode, while the released electrons pass through an external circuit (this directed movement of the electrons creates an electric current). The electrolyte allows the passage of positively charged ions. [4]

Reaction at the anode:

$$H_2 \rightarrow 2H^+ + 2e^- \quad (1)$$

At the cathode, hydrogen ions react with electrons and oxygen. The product of the reaction is water.

Reaction at the cathode:

$$\frac{1}{2}O_2 + 2H^+ + 2e^- \rightarrow H_2O \quad (2)$$

These cells operate at relatively low temperatures, around 60 ˚C - 80 ˚C. Their efficiency is about 65 % at these temperatures. Working pressure is 100 - 200 kPa. The low operating temperature has the advantage of a rapid start to electricity generation. They are able to work even below freezing. The disadvantage is the need to use precious metals such as. platinum as a catalyst. [5]

3 DESIGN OF UGV

An important part of the vehicle is a logic element (energy management system), represented by a control system responsible for managing energy flows from individual sources (battery, fuel cell, supercapacitor).

3.1 Description of the EMS function

To start the vehicle, battery power is required to turn on the control, information and communication systems. It is also used to cover the input energy requirements during the start-up of the fuel cell or during the heating of the metal hydride tank in order to release hydrogen. Hydrogen begins to enter the fuel cell under pressure.

The energy of the battery is also used for the initial movement of the vehicle. After stabilizing the energy state in the initial phase of the vehicle's movement, the EMS switches the power supply to the fuel cell. From this moment on, the entire operation of the vehicle is ensured by energy from the fuel cell. In the case of excess energy produced by the cell, this energy is stored in the accumulator or in the supercapacitor. The order of charging will depend on the current state of charge of the battery and supercapacitor.

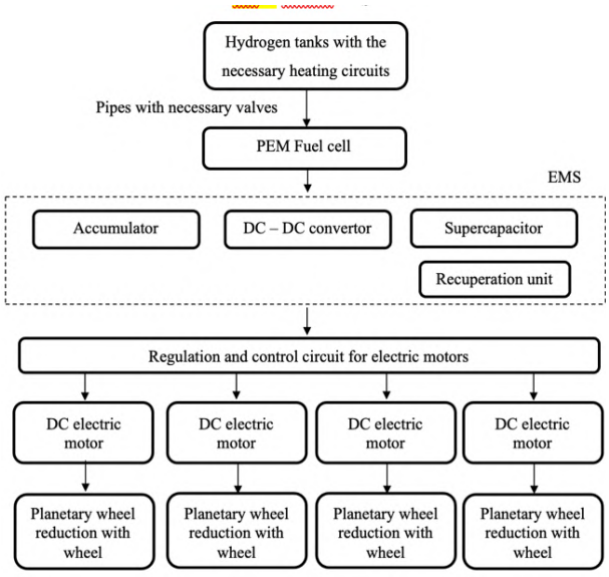

Fig. 2 Scheme of EMS
Source: authors.

If the vehicle overcomes a large incline or requires a short-term but enormous increase in energy, for example to overcome an obstacle, the energy stored in the supercapacitor will be used. On the contrary, recuperation is used during braking and the energy thus obtained is stored in the supercapacitor.

3.2 Vehicle propulsion

Due to the projected vehicle weight up to 35 kg, we choose components that are able to provide the vehicle for a given weight sufficient dynamic parameters. The vehicle uses a fixed wheel chassis without steerable axles. Each wheel is driven by its own DC motor. Turning is ensured by changing the speed of individual wheels.

3.3 DC electric motor and planetary gearbox

The vehicle has four Maxon DCX26L DC motors, which are powered by 12 V. The maximum long-term current is 4.5 A. The maximum electrical power of one DC motor is 40 W. According to the technical description, the maximum motor torque is 46.9 Nm.

The wheels are driven via a two-speed planetary gearbox, where the crown wheels are firmly connected to the vehicle structure. The drive from the DC motor is fed to the central wheel and then via the satellite carrier to the central wheel of the second gearbox. The wheel itself is directly connected to the satellite carrier. This ensures high torque on the wheels. The first planetary gearbox has a ratio of 7:1, the second 3:1. The overall gear ratio is 21:1. This slows down the engine speed and at the same time increases the torque on the wheel.

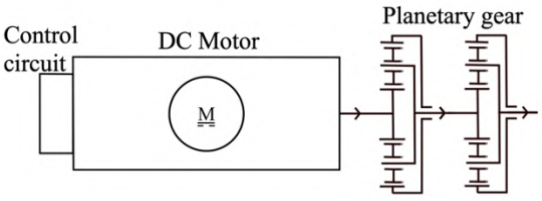

Fig. 3 Scheme of DC motor and planetary gear
Source: authors.

It follows from the theory of planetary gearboxes that the greatest torque is obtained from the planetary series just by the connection that we used, ie the central wheel as the driving element and the satellite carrier as the driven element.

To calculate the gear ratio, we must know the basic kinematic equation of the planetary gearbox, the parameter of the planet series α and the element that is driving and driven. The parameter α is calculated as the ratio of the radius of the crown r´ and the central r of the wheel, respectively as the ratio of the number of teeth of these wheels:

$$\alpha = \frac{r'}{r} = \frac{z'}{z} \quad (3)$$

The basic kinematic equation has the form:

$$n + n'.\alpha - n_o \cdot (1 + \alpha) = 0 \quad (4)$$

The variable *n* represents the speed of the central wheel, n_O the speed of the satellite carrier and n' the speed of the crown wheel. The calculation is based on the basic kinematic equation, where the constraints are determined based on the design. Our connections with the connection of the central wheel driven, the crown wheel firmly connected to the structure and the torque taken from the satellite carrier will have the shape:

$$n = n_{driving} \quad n_0 = n_{driven} \quad n' = 0$$

To calculate the gear ratio, we must adjust the basic kinematic equation to the form:

$$i = \frac{n_{driving}}{n_{driven}} \quad (5)$$

We substitute the formed bonds into the basic kinematic equation, which gives:

$$n_{ci} + 0 - n_{ný}\,(1 + \alpha) = 0 \quad (6)$$

After adjustment, we get the resulting value of the gear ratio:

$$i = \frac{n_{driving}}{n_{driven}} = 1 + \alpha \quad (7)$$

When using two planets in a row, their gear ratios are multiplied. The calculations show that to achieve a gear ratio of 7:1, the planetary line parameter must be α = 6 and for a 3:1 gear ratio, the planetary line parameter must be α = 2.

3.4 Hydrogen tank

We assume the storage of hydrogen in the form of a metal hydride. The tank is capable of holding up to 910 liters of hydrogen. Its diameter is 114 mm and height 287 mm. Weight up to 6.7 kg including hydrogen. The pressure of stored hydrogen is 1200 kPa. [6]

3.5 Fuel cell

The fuel cell used is of the PEMFC type, uses a solid electrolyte and is a low-temperature cell. The average temperature at which it operates is 35 ℃. The cell used in our vehicle forms a complete set with control circuits, coolers and the necessary voltage stabilizers from HES. The start of the cell is within 30 seconds. The maximum power is 1300 W. The given power is sufficient to cover the maximum required current and voltage for the four DC motors and at the same time has a sufficient power reserve for losses caused by voltage and current converters and stabilizers. The power reserve is also used to power all on-board systems and sensors. Hydrogen consumption at maximum output is 16.5 liters per minute. With a volume of 910 liters of hydrogen in the tank, this cell is able to operate for approximately 55 minutes at maximum power. [7]

Fig. 4 Fuel cell from HES
Source: [8].

3.6 Accumulator

The battery type is a Li-ion from Samsung with the type designation 35E. One cell has a voltage of 3.6 V and a capacity of 3,500 mAh. Long-term current, which is a battery can be used 8 A, maximum peak up to 13 A. To cover our required power, we need 24 cells, where six cells will be connected in series. The cells connected in this way are then connected in parallel, thus creating 4 parallel branches with a voltage of 21.6 V and a capacity of 14 Ah. The power provided by batteries is 691 W. With a battery, we must also take into account cooling. The battery is able to supply the required amount of current while generating heat. It is advisable to use a fan before more efficient cooling. [9]

3.7 Supercapacitor

We use six Maxwell BCAP0650 supercapacitors with a voltage of 2.6 V and a capacity of 720 F for our vehicle. The supercapacitors are connected in series, thus providing a voltage of 16.2 V and a capacity of 120 F. The stored energy is a total of 3.96 Wh. To supply the four motors we have selected, we need almost 20 A of current at 12 V. If we take into account the 80% loss caused by the DC-DC converter through which the motor drive circuit is supplied, we get to the required current value of up to 25 A. If we need to provide energy for at least 30 seconds, we need approximately 2.3 Wh of stored energy. [10]

3.8 Model of vehicle

Table 1 shows the basic parameters of the individual elements that are in the vehicle. The overall dimensions of the vehicle provide enough space for all the necessary components.

Tab. 1 Dimensions and weights of the vehicle

	Type	Length [mm]	Width/ diameter [mm]	Height [mm]	Weight [g]
Vehicle skeleton	Plastic, composite	720	300 + 170 wheels	208	8 000
Fuel cell	PEM	194	127	193	1 800
DC motor	DC	-	26.2	60	170
Planetary gear	Metal	-	22	31.7	78
Accumulator	Li-ion	-	18,55	65.25	50
Metal hydride tank	Metal	-	114	287	6 700
Supercapacitor	Maxwell	-	60.4	51	160

Source: authors.

In the construction of the vehicle, we assume the maximum use of polymer composites, which will ensure low weight and sufficient strength. Holders for all necessary elements are part of the vehicle frame. The vehicle has a low side silhouette, only 208 mm. The designed vehicle together with the basic dimensions is shown from the profile in the following figure.

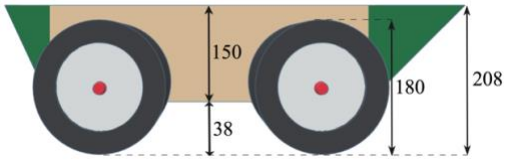

Fig. 5 Side view of UGV
Source: authors.

The wheels of the vehicle have a diameter of 18 cm and a thickness of 8.5 cm. This will ensure high vehicle throughput and sufficient traction. The large diameter of the wheels will provide enough torque to overcome obstacles.

The figure no. 6 shows the internal arrangement of the elements in the vehicle. The figure does not consider electrical circuits and pressure hoses and valves. However, they are taken into account in the design, so the model has enough space to store them.

The assumed weights of the individual elements in the vehicle and thus also the weight of the vehicle skeleton itself are in Table 2. The weight of the vehicle skeleton with all circuits and holders is approximately determined on the basis of the size of the vehicle.

Table 2 shows that the total weight of the vehicle will be 31.6 kg. When calculating the required power of DC motors and the required power of the fuel cell, batteries and supercapacitors, we used a vehicle weight of 35 kg. This has increased the weight usable for the additional components.

The power of the DC motor is 40 W. The power of the whole vehicle is 160 W. The fuel cell provides electrical power up to 1,000 W in the long run, at peak times up to 1,300 W. When calculating the required cell power, we calculated the efficiency of the DC engine itself, losses in the planetary and also in the control circuit. Losses will also be in voltage stabilizers and DC-DC converters. Therefore, we chose a cell with such a power reserve. We also confirmed the need for such a powerful cell in simulations, where weaker cells were not able to provide sufficient values of currents and voltages for the movement of the vehicle.

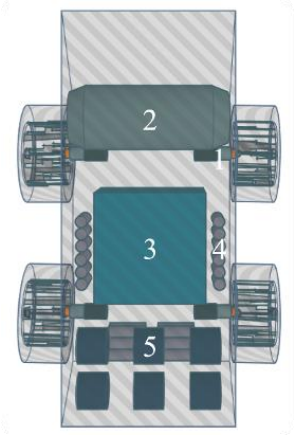

Fig. 6 Internal arrangement of the elements in the vehicle (1 – DC motor; 2 – Hydrogen tank; 3 – Fuel cell; 4 – Accumulator; 5 – Supercapacitors)
Source: authors.

Tab. 2 Total weight of the vehicle components

	Number of pieces in the design	Total weight [g]
Vehicle skeleton	1	19 000
Fuel cell	1	1 800
DC motor	4	680
Planetary gear	4	312
Accumulator	24	1 200
Metal hydride tank	1	6 700
Supercapacitor	6	960

Source: authors.

3.8 Increasing the internal volume of the vehicle

In the case of a requirement for a longer range of the vehicle, or if it is necessary to place more complex systems and sensors in the vehicle, which are more difficult to install, we can modify the design of the vehicle by adding a superstructure. Should we need to increase the service life, it is possible to add another hydrogen tank. This will increase the weight by 6.7 kg. This tank would be located above the rear axle, which would contribute to a better weight distribution. The superstructure itself weighs up to 1 kg. The vehicle profile will increase by only 50 mm, which means that the side profile of the vehicle will be 258 mm and the total weight will increase to 40 kg.

4 VEHICLE SIMULATION IN MATLAB

We performed the simulation in the Matlab program, in its Simulink toolbox, using Simscape blocks.

The overall simulation scheme contains several subsystems, in which there are individual controls and components. The subsystem facilitates orientation in individual branches.

As power source in simulation, we use fuel cell (model shown in Fig. 8) and accumulator (model shown in Fig. 9)

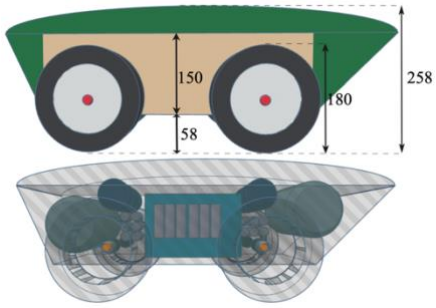

Fig. 7 Increasing the internal volume
Source: authors.

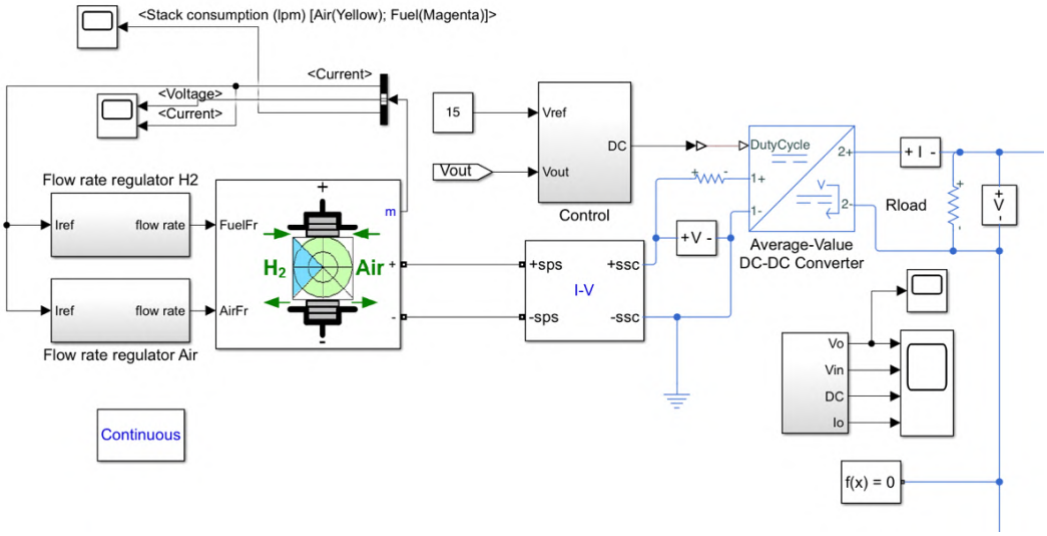

Fig. 8 Fuel cell vehicle powered model
Source: authors.

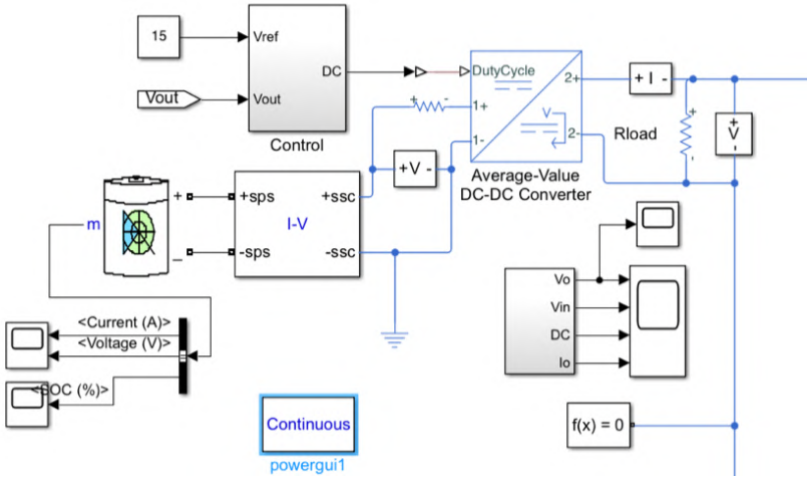

Fig. 9 Accumulator vehicle powered model
Source: authors.

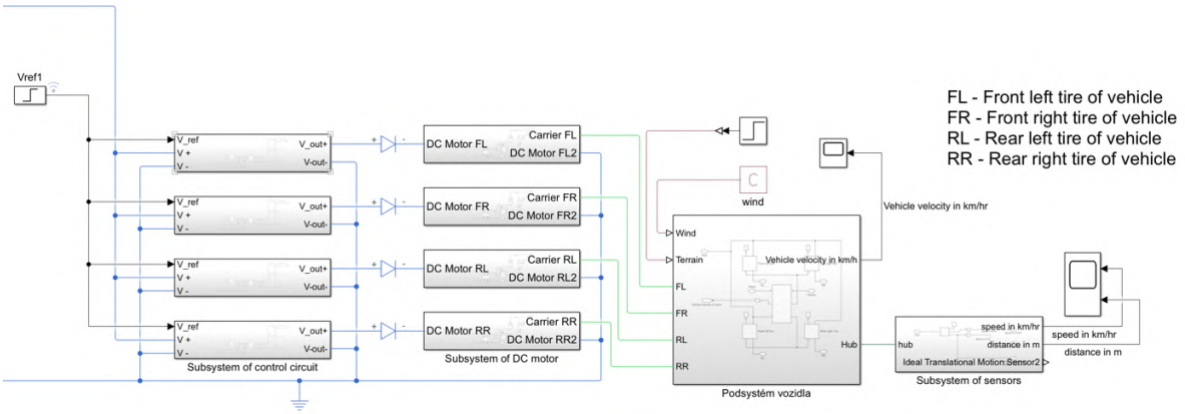

Fig. 10 Model of a 4-wheeled vehicle platform with electric motors and their regulators
Source: authors.

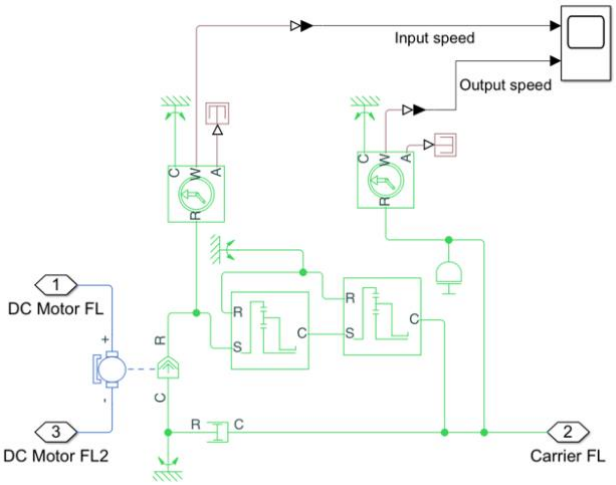

Fig. 11 Detailed view of the model of the DC motor - planetary gearbox subsystem
Source: authors.

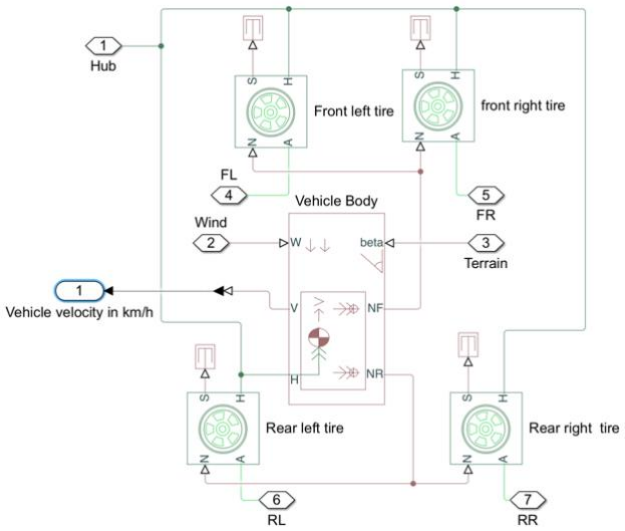

Fig. 12 Detailed view of the model of the vehicle's 4-wheel platform subsystem
Source: authors.

The parameters for each component were set by technical data sheets. The efficiencies of the converters are 80 %. We brought the simulation as close as possible to the real conditions and we set all resistances and inertia values as accurately as possible and as close as possible to the real values. We used a proportional integration (PI) controller to control individual DC motors according to referenced voltage, in our model simulated by source of signal, in Fig. 10 marked as "Vref1"

5 SIMULATION RESULTS

First, we will show a simulation of a vehicle powered by a fuel cell at 12 V, reducing the voltage to 6 V after 90 seconds. The simulation time is 180 seconds, which is enough time to stabilize the speed at a given voltage. Voltage changes are only made on the DC motor control circuit. Since the control system is connected, the fuel cell also responds to the change. From the fuel cell we get a voltage of 15 V. This is due to the reserve for powering the control circuit of the DC motor, which is realized through a DC DC converter with an efficiency of 80 %.

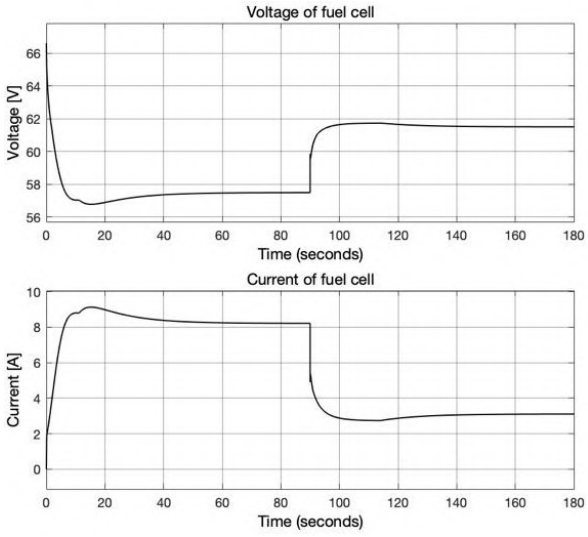

Fig. 13 Graph of FC voltage and current when changing power supply of motors from 12 V to 6 V
Source: authors.

When the vehicle is started and 12 V is consumed, the motors consume almost 9 A. The voltage drops from an initial voltage of 66 V to 57 V. At a steady speed, the current consumption is stabilized at 8 A and the voltage at 57.5 V. When the required voltage changes from 12 V to 6 V, the current consumption drops to less than 3 A. The voltage rises to 62 V.

At the start it is necessary to overcome a large torque and thus the current rises and as we have loaded the power source, its voltage decreased.

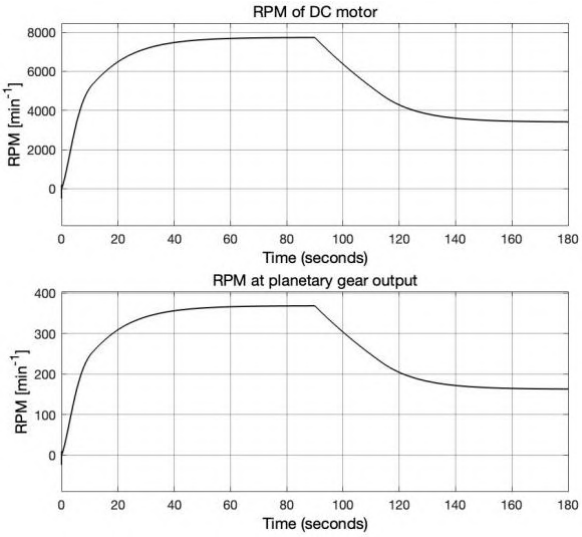

Fig. 14 Graph of gearbox speed when changing the supply voltage of motors from 12 V to 6 V
Source: authors.

The motor speed is at a voltage of 12 V and at a steady current of 4 A approximately 7800 min ^{1}, the output speed is reduced 21 times, approx. 371 min$^{-1.}$

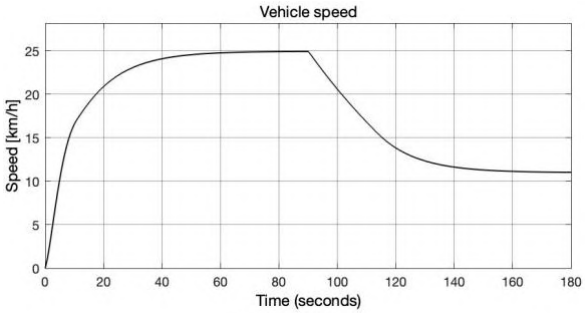

Fig. 15 Graph of vehicle speed when changing the power supply of motors from 12 V to 6 V
Source: authors.

The vehicle speed stabilized at 25 km / h at 12 V on the DC motor, which is the maximum vehicle speed. When changing to 6 V, the speed dropped to approximately 10.5 km / h. This change represents the functionality of the control circuit. By changing the speed of the individual wheels, we are able to turn.

Next, we will simulate the situation of changing the supply voltage from 6 V to 12 V. The input conditions are the same as in the simulation. The voltage at the output of the fuel cell is given by a DC-DC converter to 15 V, the voltage at the DC motor is initially 6 V and after 90 seconds it changes to 12 V.

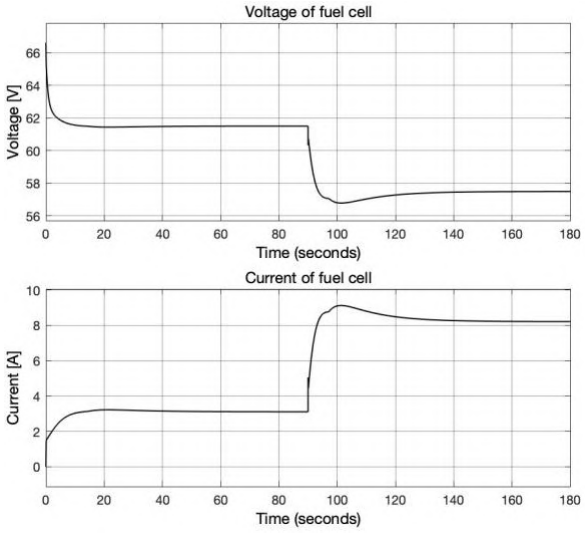

Fig. 16 Graph of FC voltage and current when changing power supply of motors from 6 V to 12 V
Source: authors.

When the vehicle is started and DC motors 6V and 3.2 A are consumed, the FC voltage drops from an initial voltage of 66 V to 61.8 V. When the required voltage changes from 6 V to 12 V, the voltage drops below 57 V and the voltage is maintained when the speed stabilizes. at 57.5 V. In 90 seconds, the current consumption rises to 9 A and drops to 8.1 A after stabilizing the speed.

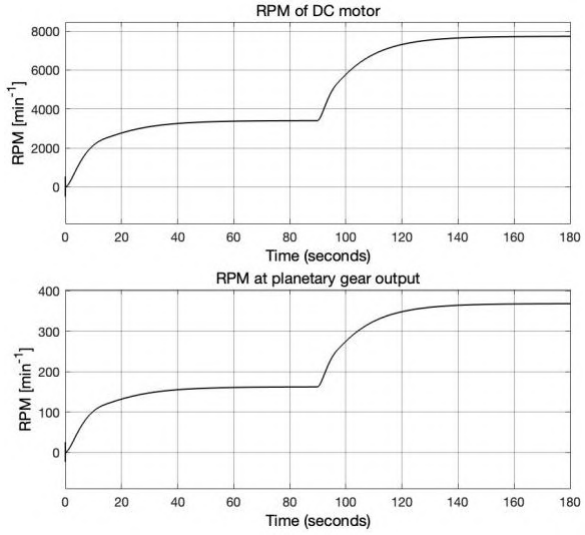

Fig. 17 Graph of gearbox speed when changing the supply voltage of motors from 6 V to 12 V
Source: authors.

The speed at the output and output of the gearbox changed as expected. At the beginning of the graphs, however, we can notice large changes in the speed of both the DC motor and the gearbox. This change is very short, in the order of tenths of a second. This fluctuation would probably not occur in real conditions.

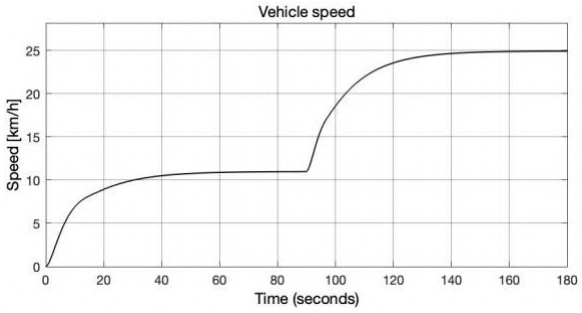

Fig. 18 Graph of vehicle speed when changing the power supply of motors from 6 V to 12 V
Source: authors.

The initial speed at 6 V stabilized at approximately 10.5 km / h, increasing to 12 V reached a maximum vehicle speed of 25 km / h.

6 CONCLUSION

It was verified by simulation that a vehicle weighing about 32 kg is able to reach a maximum speed of 25 km/h using a fuel cell - due to the capacity of the tank, for 55 minutes. As the vehicle does not move at this speed continuously, the operating time is extended even further. If a second hydrogen tank (with the same volume as the first tank) is also installed in the vehicle, the operating time will be doubled.

If operating time is a priority for the use of UGV, then a fuel cell-based energy source is a better solution than a lithium battery.

References

[1] SPIRIDIGLIOZZI, L. *Doped-Ceria Electrolytes*. Cassino (Taliansko): University of Cassino and Southern Lazio, 2018. 80 s. ISBN 978-3-319-99395-9.

[2] INTERNATIONAL ENERGY AGENCY. *Hydrogen & fuel cells*. Paris: Head of Publications Service, OECD/IEA, 2004. 204 s. ISBN 92-64-108-831.

[3] CODINA, A. *System Level modelling of fuel cell driven electric vehicles* : diplomová práca. Gothenburg: Chalmers university of technology, 2017. 66 s.

[4] HORÁK, S. *Palivové články a jejich použití :* diplomová práca. Brno: Vysoké učení technické v Brně, 2012. 46 s.

[5] KUBICA, J. *Návrh modelu palivového článku* : bakalárska práca. Bratislava: Slovenská technická univerzita v Bratislave, 2005. 43 s.

[6] FUEL CELL STORE. CL – 910 Metal Hydride [online]. [cit. 2020-09-30]. Available at: https://www.fuelcellstore.com/cl-910-metal-hydride.

[7] HES ENERGY SYSTEMS. Aerostak A – 1000 [online]. [cit. 2020-09-30]. Available at: https://www.hes.sg/aerostak.
[8] FUEL CELL STORE. Aerostak A – 1000-HV (Ultralight 1000 W High Voltage PEM Fuel Cell System) [online]. [cit. 2020-05-18]. Available at: https://www.fuelcellstore.com/fuel-cell-stacks/medium-power-fuel-cell-stacks/aerostak-a-1000-hv-ultralight.
[9] VAPO CITY. 3500mAh Samsung 18650 INR18650-35E up to 13A [online]. [cit. 2020-09-30]. Available at: https://www.vapo-city.de/3500mAh-Samsung-18650-INR18650-35E-up-to-13A.
[10] MAXWELL TECHNOLOGIES. 2.7V 650-3000F ultracapacitor cells [online]. [cit. 2020-09-30]. Available at: https://www.maxwell.com/images/documents/K2Series_DS_1015370_5_20141104.pdf

Dipl. Eng. Vladimír **POPARDOVSKÝ**, PhD.
Armed Forces Academy of General M. R. Štefánik
Department of Mechanical Engineering
Demänová 393
031 01 Liptovský Mikuláš
Slovak Republic
E-mail: vladimir.popardovsky@aos.sk

Dipl. Eng. Peter **BONDRA**
Armed Forces Academy of General M. R. Štefánik
Department of Mechanical Engineering
Demänová 393
031 01 Liptovský Mikuláš
Slovak Republic
E-mail: bondra.peter@gmail.com

Dipl. Eng. Lukáš **NOVOTNÝ**
Armed Forces Academy of General M. R. Štefánik
Department of Mechanical Engineering
Demänová 393
031 01 Liptovský Mikuláš
Slovak Republic
E-mail: novotn.lukas@gmail.com

Vladimír Popardovský works at the Department of Mechanical Engineering, Armed Forces Academy in Liptovský Mikuláš. He received his engineer degree from the Faculty of Chemical Technology, Slovak Technical University in Bratislava in 1994. He received a Ph.D. degree from the Faculty of Electrical Engineering and Information Technology, Slovak Technical University in Bratislava in 2000. His research interest is advanced automatic control of mechanical and electrochemical systems.

Peter Bondra is currently an air traffic controller at the international airport Sliač in the middle of Slovakia. He received his engineer degree in 2020 in Weapons systems, weapons and their components from Department of Mechanical Engineering, Armed Forces Academy in Liptovský Mikuláš He is interested in aviation, mechanics and engines.

Lukáš Novotný is the PhD. student at the Department of Mechanical Engineering, Armed Forces Academy in Liptovský Mikuláš. He received his engineer degree in 2017 in Armament and technics of military forces from Department of Mechanical Engineering, Armed Forces Academy in Liptovský Mikuláš. His research area is fuel cell technology in military applications.

DOI: https://doi.org/10.52651/sam.a.2021.1.14-18

DILATOMETRIC ANALYSIS TOOL STEEL X153CRMOV12

Michal KRBAŤA, Róbert CÍGER

Abstract: The article deals with phase transformations and austenitizing behavior of the X155CrMoV12 tool steel. Dilatation analyses of a series of samples were performed at various cooling rates, chosen in the range from 10 °C·s^{-1} to 0.1 °C·s^{-1}. Acquired experimental data were used for evaluation of dilatometric curves in order to map the temperature ranges of phase transformations of the austenite to pearlite, bainite or martensite. All experimental samples from dilatometric analyses were then subjected to microstructural analyses and hardness measurements to characterize the microstructure and hardness for every tested heat treatment regime. The second part of this article, entitled "EXPERIMENTAL DETERMINATION OF CONTINUOUS COOLING TRANSFORMATION DIAGRAM FOR HIGH STRENGTH STEEL X153CRMOV12", deals with these analyses of the cooling curve microstructure.

Keywords: ARA diagram; Tool steel; Dilatometry; Compression test.

1 INTRODUCTION

Some currently produced steels with extreme high content of carbide forming elements are known as ledeburitic steels. Ledeburitic structure is typical for white cast irons with carbon content above 2.11 wt. % as is shown in the Fe-Fe_3C metastable binary diagram in Fig. 1 [1, 2]. However, alloying element present in the ledeburitic steel extend the area of the ferrite and narrow area of the austenite. Consequently, the eutectoid point S and the point of maximum solubility of carbon in austenite – E are moved to the lower carbon content values. Due to this effect, ledeburite is present in structure of these steels at carbon content below 2.11 wt. %. Common carbon content in ledeburitic steels is higher than 0.7 wt. %. At lover carbon content, there would be present a certain amount of δ-ferrite, negatively influencing the hardness [3].

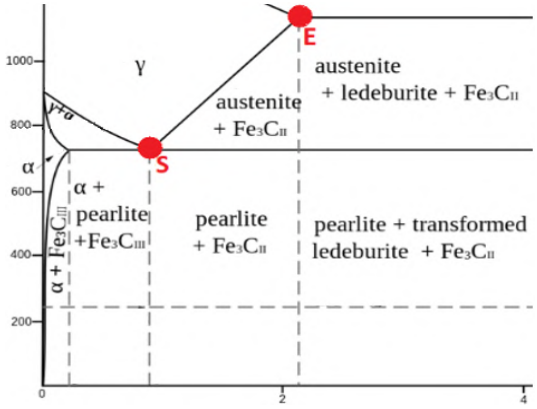

Fig. 1 Selected part of phase diagram Fe-Fe_3C binary system
Source: authors.

2 MATERIALS AND METHODS

The experimental material used in these experiments is high-alloy tool steel X153CrMoV12 used in the engineering industry. It is a high hardenability chromium-vanadium steel suitable for oil and air hardening [4]. Steel is characterized by high wear resistance and is mostly used for cutting tools such as tensioning and extrusion mandrels, profile sheets and complex shaped cutters. The chemical composition of the experimental samples was verified with a TASMAN Q4 spectrum analyser and is listed in Tab. 1. Its basic mechanical and physical properties are listed in Tab. 2.

Tab. 1 Chemical composition of steel X153CrMoV12 (wt.%)

Element	Min - Max	Spectral analysis
C	1.45-1.60	1.53 ± 0.01
Mn	0.20-0.60	0.21 ± 0.005
Si	0.10-0.40	0.14 ± 0.005
Cr	11.00-13.00	12.25 ± 0.02
Mo	0.70-1.00	0.89 ± 0.01
V	0.70-1.00	0.76 ± 0.01

Source: authors.

Tab. 2 Basic mechanical and physical properties of X153CrMoV12 steel

Mechanical and physical properties	Value
Tensile strength (MPa)	650 - 880
Modulus of elasticity (GPa)	198
Thermal conductivity (W·m^{-1}·K^{-1})	25
Hardness (HV)	790
Specific therm. capacity (J·kg^{-1}·K^{-1})	460

Source: authors.

The base material was supplied in the form of bars with a diameter of 10 mm and a length of 1000 mm. The supplied material is produced in electric furnaces

with the possibility of treatment of liquid steel in secondary metallurgy units. The base material was in a soft annealed state with heating to a temperature just below. Ac1 in the whole cross section, followed by cooling in an oven at a rate of 20 °C/h with a maximum hardness of 270 HV. The microstructure of the base preparation showed a distribution of course and fine spheroidized carbide particles in the ferrite matrix, which is highly machinable and offers less resistance to deformation compared to other microstructures formed during hardening of tool steels.

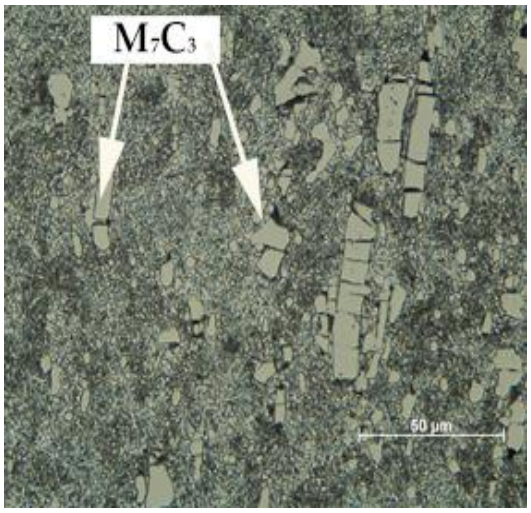

Fig. 2 Basic microstructure of X153CrMoV12 in the normalized state observed-LOM
Source: authors.

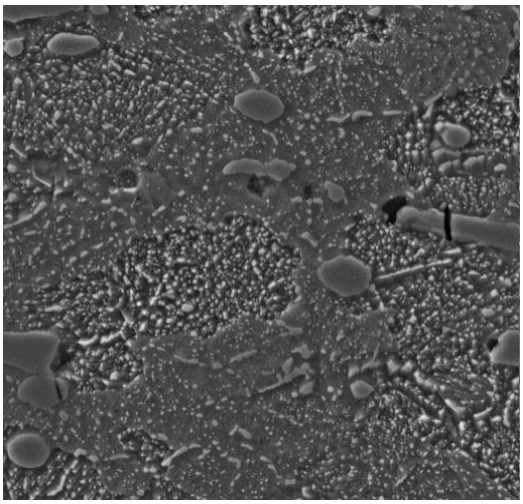

Fig. 3 Basic microstructure of X153CrMoV12 in the normalized state observed-SEM
Source: authors.

The larger particles of distributed spheroidized carbides shown in Fig. 2 and Fig. 3 are primary M_7C_3 carbides that formed during solidification and that dispersed because of heat treatment. Finer carbides ($M_{23}C_6$) originate from secondary precipitation in the spherodization of carbides produced by the transformation of austenite to the microstructure of ferrite carbides by cooling after earlier normalization of the heat treatment (Fig. 4).

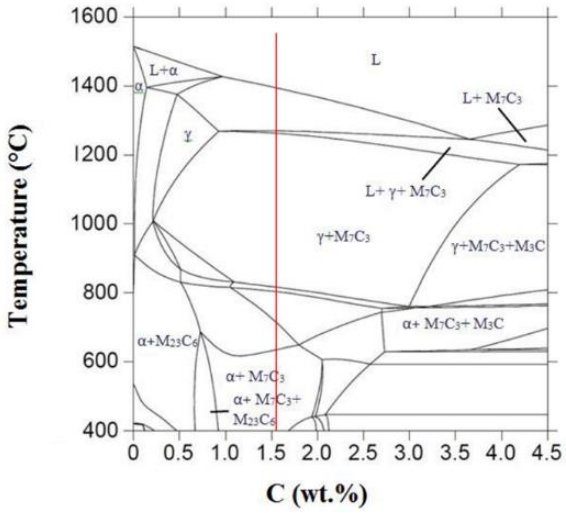

Fig. 4 Calculated phase diagram for X153CrMoV12 steel
Source: authors.

3 RESULT AND DISCUSSION

Phase change occurs in the dilatation curve as a step change in length of the experimental sample. For example, critical temperature Ac_1 corresponds with temperature where the sample starts to contract due to the austenite formation in contrast to the linear expansion during heating. Then, the Ac_3 critical temperature is defined as a temperature where the expansion of the sample starts to be linear again. Heating conditions were the same for all experimental samples, therefore the initial and final austenitizing critical temperatures are constant. Their values for X153CrMoV12 steel are Ac_1=820 °C and Ac_3=850 °C and can be seen in Fig. 5 and Fig. 6.

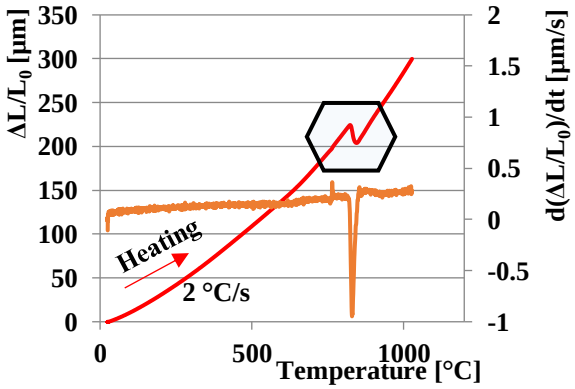

Fig. 5 Determination of transition temperatures Ac_1 and Ac_3 with continuous heating at 2 °C·s^{-1}
Source: authors.

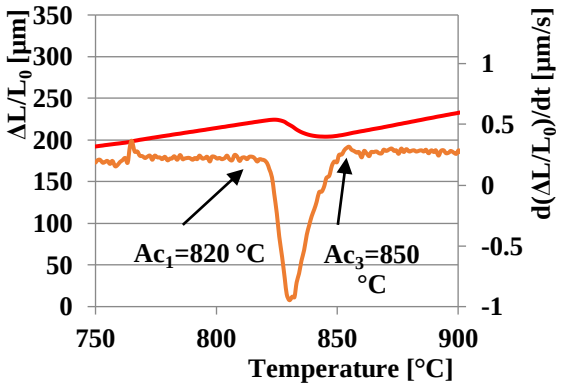

Fig. 6 Increase the area of the expansion curve with Ac_1 and Ac_3
Source: authors.

In Fig. 7, there are visible cooling curve and microstructure of the sample cooled at the rate of 10 °C·s^{-1}. According to dilatometry, Ms temperature was determined as 260 °C (Fig. 7). This temperature represents a rate when only the martensitic matrix and the excluded carbides appear in the structure. The following figure (Fig. 8) the results for sample cooled with rate of 5 °C·s^{-1} are shown. There was observed martensite formation start at 260 °C. In the given curve, the first slight decrease is visible through the derivation, which represents the beginning of the bainite formation immediately followed by the second decrease, which represents the instant formation of the martensite.

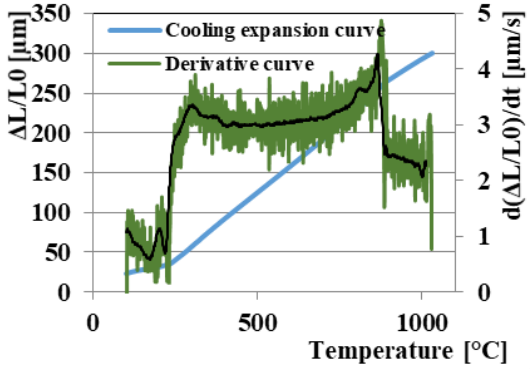

Fig. 7 Analysis of the cooling curve 10 °C·s^{-1}
Source: authors.

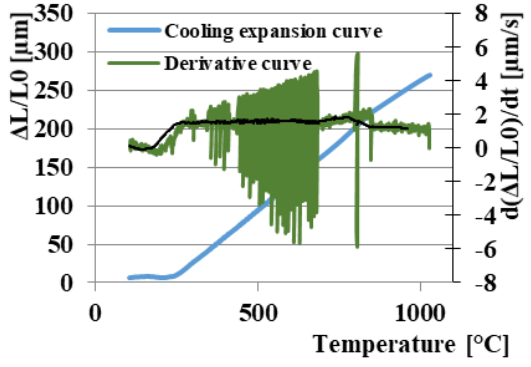

Fig. 8 Analysis of the cooling curve 5 °C·s^{-1}
Source: authors.

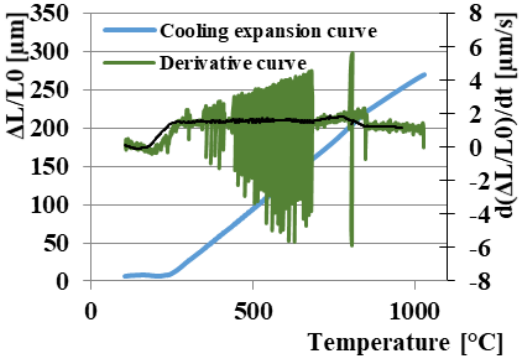

Fig. 9 Analysis of the cooling curve 3 °C·s^{-1}
Source: authors.

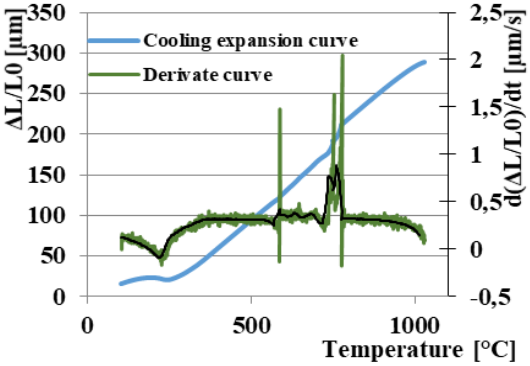

Fig. 10 Analysis of the cooling curve 1 °C·s^{-1}
Source: authors.

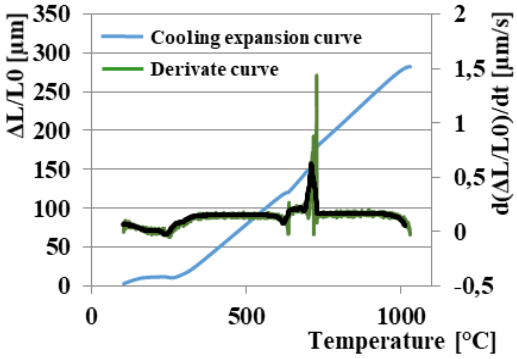

Fig. 11 Analysis of the cooling curve 0.5 °C·s^{-1}
Source: authors.

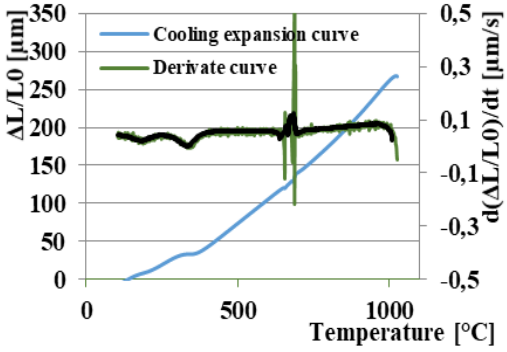

Fig. 12 Analysis of the cooling curve 0.2 °C·s^{-1}
Source: authors.

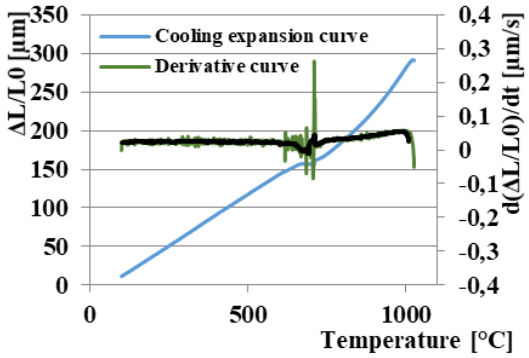

Fig. 13 Analysis of the cooling curve 0.1 °C·s^{-1}
Source: authors.

Further cooling curve (Fig. 9) represents a cooling rate of 3 °C·s^{-1}. In the length change curve, two transitions of transformation are visible. The first one began at 290 °C, which indicates the start of bainite formation and the second at 262 °C, which represents the transformation to martensite. From the derivation of the curve, precipitation of carbides is visible at 585 °C. At a cooling rate of 1 °C·s^{-1}, the bainite formation started at 340 °C. The martensite formation was shifted to 297 °C (Fig. 10). Furthermore, a cooling rate of 0.5 °C·s^{-1} was evaluated (Fig. 11). The beginning of the precipitation of the carbides is visible in the dilatation curve at 689 °C. The bainite formation began at 350 °C and the final transformation to martensite was visible below 250 °C. The next cooling rate was set to 0.2 °C·s^{-1} (Fig. 12). The precipitation of the carbides started at 689 °C. Bainite transformation Bs started at 400 °C and the martensite transformation temperature Ms was 300 °C. The results from the lowest cooling rate (0.1 °C·s^{-1}) are visible in Fig. 13. At the beginning of the cooling, which is the area of the start of the pearlite formation Ps from the austenite. The start of the transformation occurred at 705 °C and its end Pf was at 648 °C. As the dilatation curve continues, a transition through a bainitic transformation begins at a temperature of 430 °C. The transformation to martensite is no longer visible on the dilatometric curve. Therefore, it is possible to predict that the bainitic and martensitic transformation was associated, i.e. the limit value of the transformation to martensite is occurred.

4 CONCLUSION

The phase transformation kinetics under continuous cooling conditions was examined in detail using dilatometry. The higher percentage of chromium in the material results in the formation of Cr_7C_3 carbide, which results in an increased value of the hardness of the material [5, 6]. Provided the martensitic transformation is achieved, the resulting critical cooling rate is set at 5 °C·s^{-1}. This rate, which is precisely bordered by the literature sources, suggests that triple tempering should be followed to achieve the resulting uniform structure of the material. The results of chromium carbides show a fact, that at high cooling rates the incidence of hard carbides is occurred.

References

[1] JURČI, P. *Nástrojové ocele ledeburitického typu (Ledeburitic tool steels).* Praha: CVUT, 2009. p. 221–225. ISBN 978-80-01-04439-1.

[2] YANG, J., B. CAO, Y. WU, Z. GAO and R. HU. Continuous cooling transformation (CCT) behavior of a high Nb-containing TiAl alloy. In: *Acta Materialia*. 2019, **5**(17), p. 1589–1599. ISSN 2589-1529. Available at: https://doi.org/10.1016/j.mtla.2018.11.018

[3] JURČI, P. and L. JANKA. Wear resistance of sub-zero processed Cr-V ledeburitic steel vanadis 6. In: *Metal 2012: 21st International Conference on Metallurgy and Materials*. 2012, p. 635-639. ISBN 978-80-87294-29-1.

[4] BERKOWSKI, L. The influence of warm plastic deformation on the structure and on the applicable properties of highspeed steel. In: *Journal of Materials Processing Technology*. 1996, **60**(1-4), p. 637-641. ISSN 0924-0136. Available at: https://doi.org/10.1016/0924-0136(96)02398-9

[5] ECKERT, M. *Analýza a modelovanie správania sa nástrojových ocelí pri tvárnení za tepla* (Analysis and modeling of hot forming behavior of tool steels). Trenčín: Trenčianska univerzita A. Dubčeka, 2020. p. 90.

[6] ECKERT, M., M. KRBAŤA, I. BARÉNYI, J. MAJERÍK, A. DUBEC and M. BOKES. Effect of selected cooling and deformation parameters on the structure and properties of AISI 4340 steel. In: *Materials*. 2020, **13**(23), p. 5585-5606. ISSN 1996-1944. Availale at: https://doi.org/10.3390/ma13235585

Dipl. Eng. Michal **KRBAŤA**, PhD.
Department of Engineering Technologies and Materials
Faculty of Special Technology
Alexander Dubček University of Trenčín
Ku kyselke 469
911 06 Trenčín
Slovak Republic
E-mail: michal.krbata@tnuni.sk

Dipl. Eng. Róbert **CÍGER**
Department of Engineering Technologies and Materials
Faculty of Special Technology
Alexander Dubček University of Trenčín

Ku kyselke 469
911 06 Trenčín
Slovak Republic
E-mail: robert.ciger@tnuni.sk

Michal Krbaťa – was born in Trenčín, Slovakia in 1988. He received his Master and PhD. degrees at Alexander Dubček University of Trenčín, Faculty of Special Technology in Trenčín. In his research he focuses on materials research, tribology and dilatometry.

Róbert Cíger – was born in Trenčín, Slovakia in 1996. He received his Master degrees at Alexander Dubček University of Trenčín, Faculty of Special Technology in Trenčín. In his research he focuses on materials research, dilatometry.

DOI: https://doi.org/10.52651/sam.a.2021.1.19-24

EXPERIMENTAL DETERMINATION OF CONTINUOUS COOLING TRANSFORMATION DIAGRAM FOR HIGH STRENGTH STEEL X153CRMOV12

Michal KRBAŤA, Róbert CÍGER

Abstract: The article is a continuation of the article ‚DILATOMETRIC ANALYSIS OF COOLING CURVES FOR HIGH STRENGTH STEEL X153CrMoV12", which deals with the phase transformations of tool steel X153CrMoV12. The experimental data obtained was used to evaluate the resulting CCT diagram, which consists of seven dilation curves. All experimental samples from dilatometric analyses were then subjected to microstructural analysis and hardness measurements to characterize the microstructure and hardness for each heat treatment mode tested. AFM microscopy was also used to study the carbides present in steels and their size and shape for all selected cooling modes.

Keywords: Dilatometry; Tool steel; Cooling rate; Martensite; CCT diagram.

1 INTRODUCTION

In practical situations, Continuous Cooling Transform (CCT) diagram play an important role in the development of high-strength advanced steels. The CCT diagrams allow accurate predictions of the microstructures compositions that may arise in the real processing of these steels. They are generally used to design and optimize special heat treatments and predict the resulting microstructures and mechanical properties [1, 2]. These phase transformation curves provide precise information about microstructure resulting from non-isothermal austenite decomposition.

The resulting diagrams serve the needs of the metallurgical industry for further heat treatment of steel. Unfortunately, the availability of CCT diagrams created for transformation of intercritical austenite practically does not exist in open literature and therefore the mechanisms of transformation are not fully understood. Respectively, diagrams can be obtained using various software, but their use is more informative than scientific, since all of these software have to limit their field of activity many times by the percentage limitation of the chemical composition of steels.

2 MATERIALS AND METHODS

The experimental material used in these experiments is high-alloy tool steel X153CrMoV12 used in the engineering industry. It is a high hardenability chromium-vanadium steel suitable for oil and air hardening. Steel is characterized by high wear resistance and is mostly used for cutting tools such as tensioning and extrusion mandrels, profile sheets and complex shaped cutters.

The chemical composition of the experimental samples was verified with a TASMAN Q4 spectrum analyser and is listed in Tab. 1. Its basic mechanical and physical properties are listed in Tab. 2.

Tab. 1 Chemical composition of steel X153CrMoV12 (wt.%)

Element	Min - Max	Spectral analysis
C	1.45-1.60	1.53 ± 0.01
Mn	0.20-0.60	0.21 ± 0.005
Si	0.10-0.40	0.14 ± 0.005
Cr	11.00-13.00	12.25 ± 0.02
Mo	0.70-1.00	0.89 ± 0.01
V	0.70-1.00	0.76 ± 0.01

Source: authors.

Tab. 2 Basic mechanical and physical properties of X153CrMoV12 steel

Mechanical and physical properties	Value
Tensile strength (MPa)	650 - 880
Modulus of elasticity (GPa)	198
Thermal conductivity ($W \cdot m^{-1} \cdot K^{-1}$)	25
Hardness (HV)	790
Specific therm. capacity ($J \cdot kg^{-1} \cdot K^{-1}$)	460

Source: authors.

2.1 Atomic force microscopy

Images were directly obtained using the MFP-3D Infinity AFM microscope (Oxford Instruments). Surface scanning was realized using the AC Air Topography mode, where the cantilever tip is not in constant contact with the tested surface but is vibrates near its resonance frequency and tapes the surface to obtain information of the topography of the tested sample surface. Since this is a relatively high-strength sample, the AC 160TS-R3 cantilever with the spring constant 26 $N.m^{-1}$, resonance frequency 300 Hz and the tip radius in range 5 – 10 nm was used for all performed measurements [3, 4].

3 MICROSTRUCTURE

As is already known, the austenite decomposition and finally formed phases depend on cooling rate. This course of austenite decomposition during continuous cooling corresponds to the discontinuity of the slope detected in the dilatometric curves and is related to the temperature range of specific microstructure type formation. Although the temperature ranges, in which the various phase transformations in the steel can occur, are relatively wide and may even overlap, every phase transformation occurred during the overall continuous cooling process could be detected. The microstructure of the first 10 °C·s^{-1} cooling curve was evaluated as martensitic. Ms temperature was determined as 260 °C. This temperature represents a rate when only the martensitic matrix and the excluded carbides appear in the structure (Fig. 1). In the figure from the AFM microscope, the grain boundaries are clearly visible. In the figure, there are visible small white areas, representing the carbides, and the dark circular areas, representing the holes that have arisen as the carbides ripped from the matrix during grinding process (Fig. 2). Metallographic analysis of the second cooling curve 5 °C·s^{-1} revealed the occurrence of Cr_7C_3 carbides, the martensitic matrix (Fig. 3). As can be seen in the previous figure, the grain boundaries and the primary carbides are clearly visible through the AFM microscope. Only few amounts of bainite have already occurred (Fig. 4). At a third cooling curve of 3 °C·s^{-1}, the incidence ratio of Cr_7C_3 carbides decreased compared to previous cooling rates (Fig. 5, Fig. 6). The matrix was composed of martensite and bainite. At the cooling rate of 1 °C·s^{-1}, a greater amount of bainite than martensite was present in the microstructure. There was still a small amount of Cr_7C_3 chromium carbides in the matrix (Fig. 7, Fig. 8) and the metallographic analysis showed the same occurrence of structures as the expansion of curves. Metallographic analysis shows that at the cooling rate of 0.5 °C·s^{-1}, the morphology of the carbides in the sample was changed to coarse-grained (Fig. 9, Fig. 10). The matrix was predominantly bainite with a low incidence of martensite. In the metallographic analysis (Fig. 11, Fig. 12) in addition to the carbides, about 15 % of pearlite structure was found but was not observed in the dilatation curve. Fe_3C carbides precipitated inside of the matrix grains. The AFM microscope shows a surface topography that confirms the occurrence of a coarse-grained structure. In the last cooling curve, which had the slowest cooling rate of 0.1 °C·s^{-1}, the bainitic and martensitic transformation were connected at the end of the curve, for the martensitic transformation was its limit value. It can be assumed that the device did not notice this change due to a very small change in material volume. In this case, the resulting structure was pearlite with coarsely precipitated Fe_3C carbide according to metallographic analysis (Fig. 13, Fig. 14). Further measurements were not performed because all resulting types of microstructures were achieved.

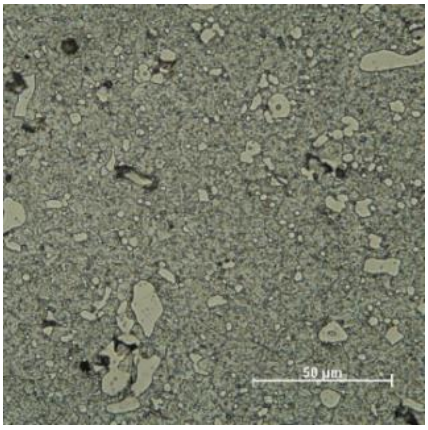

Fig. 1 Microstructure of the cooling curves 10 °C·s^{-1}
Source: authors.

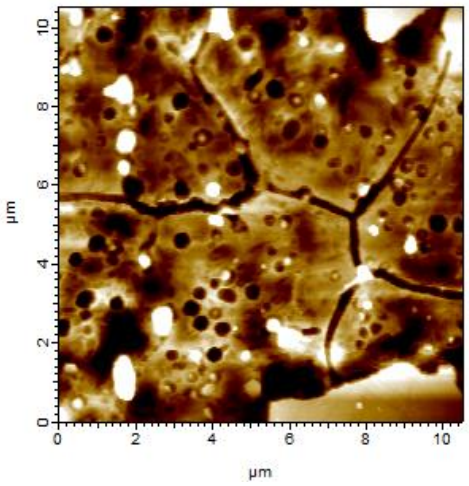

Fig. 2 Surface topography by AFM 10 °C·s^{-1}
Source: authors.

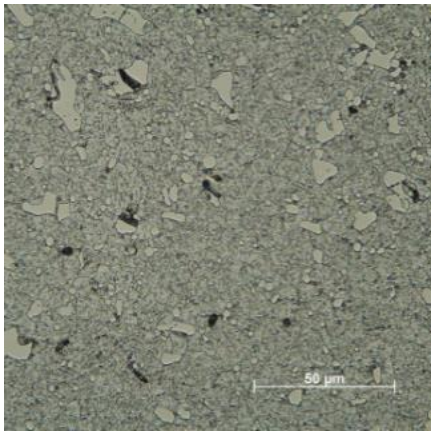

Fig. 3 Microstructure of the cooling curves 5 °C·s^{-1}
Source: authors.

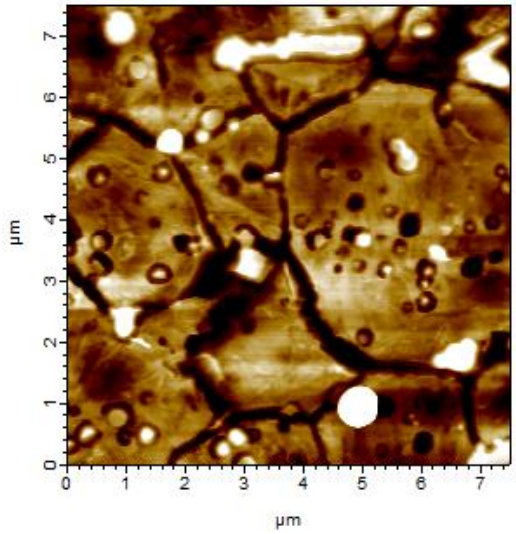

Fig. 4 Surface topography by AFM 5 °C·s^{-1}
Source: authors.

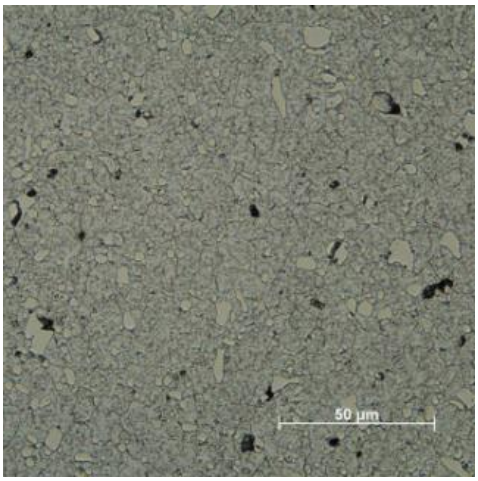

Fig. 5 Microstructure of the cooling curves 3 °C·s^{-1}
Source: authors.

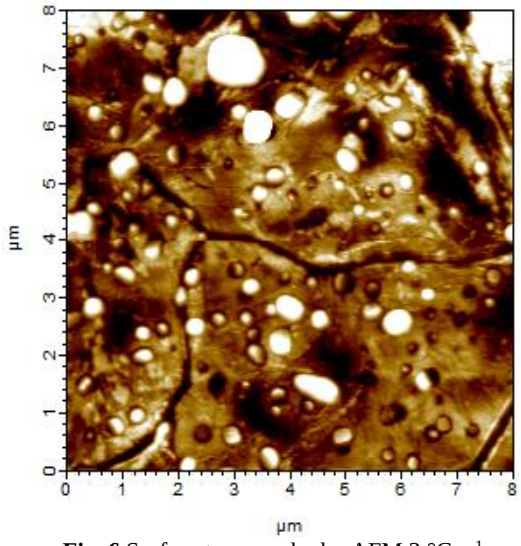

Fig. 6 Surface topography by AFM 3 °C·s^{-1}
Source: authors.

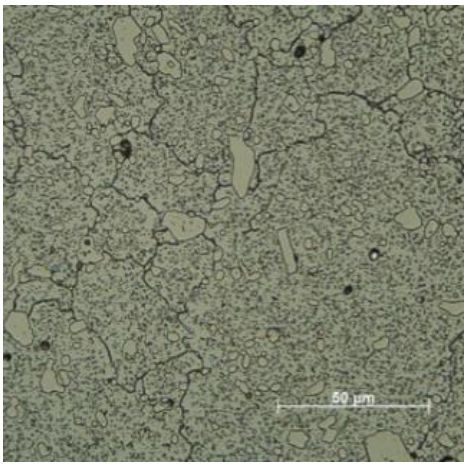

Fig. 7 Surface topography by AFM 1 °C·s^{-1}
Source: authors.

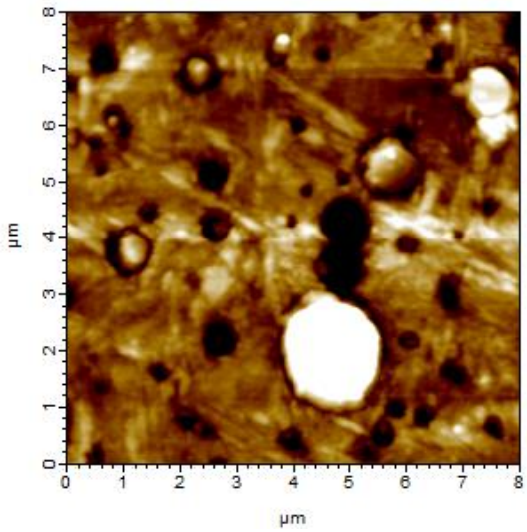

Fig. 8 Surface topography by AFM 1 °C·s^{-1}
Source: authors.

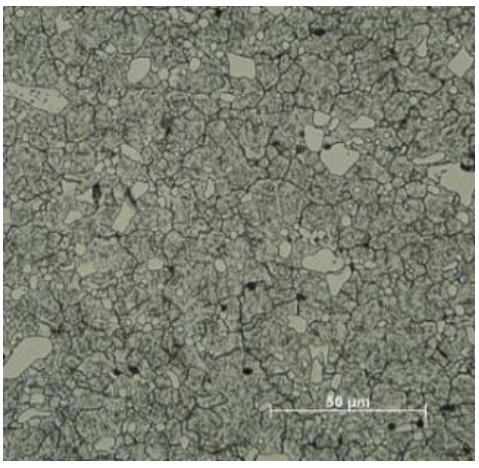

Fig. 9 Surface topography by AFM 0.5 °C·s^{-1}
Source: authors.

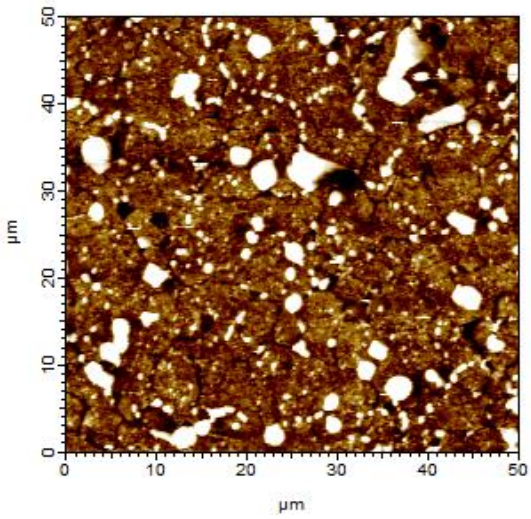

Fig. 10 Surface topography by AFM 0.5 °C·s^{-1}
Source: authors.

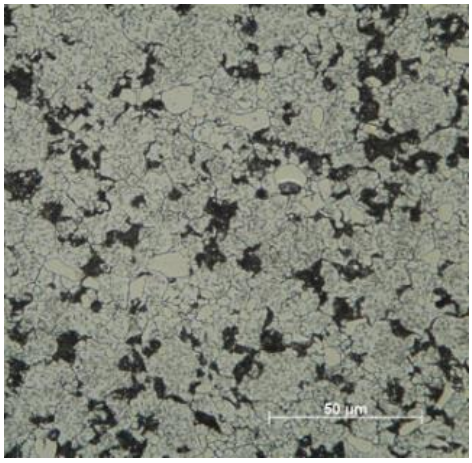

Fig. 11 Surface topography by AFM 0.2 °C·s^{-1}
Source: authors.

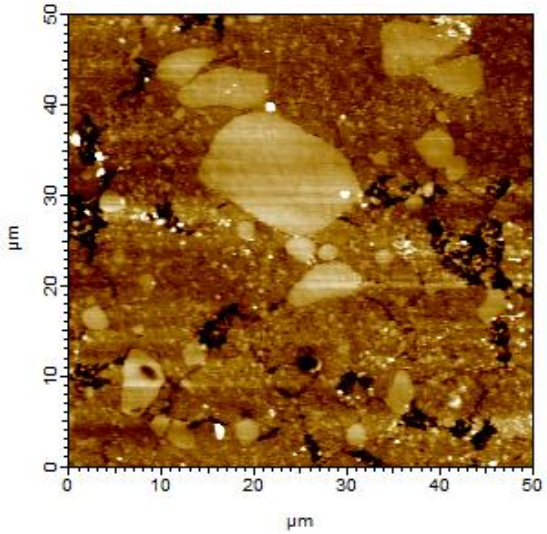

Fig. 12 Surface topography by AFM 0.2 °C·s^{-1}
Source: authors.

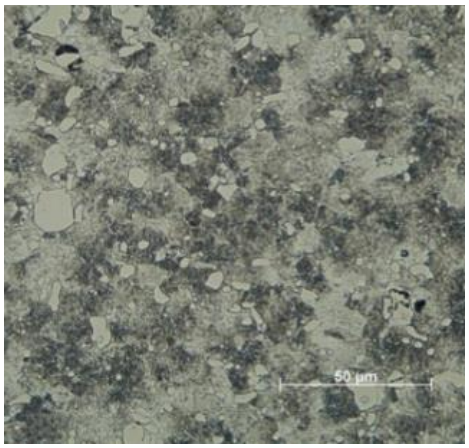

Fig. 13 Surface topography by AFM 0.1 °C·s^{-1}
Source: authors.

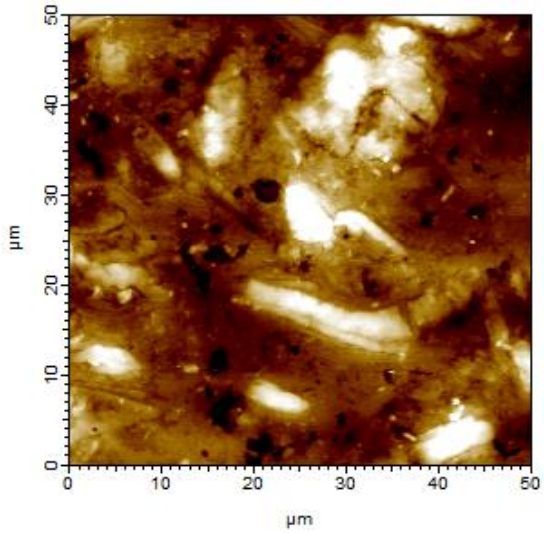

Fig. 14 Surface topography by AFM 0.1 °C·s^{-1}
Source: authors.

4 CCT DIAGRAM OF X153CRMOV12 STEEL

The diagram was constructed from all measured data, i.e. all seven cooling curves. The diagram clearly shows areas of austenite transformation to bainite and martensite. Consequently, at the top we can see the area of pearlitic transformation [5, 6, 7, 8]. Striped red lines mark the temperatures Ac_1 and Ac_3, which point to the transformation of the initial state microstructure to austenite while heating of the sample. A long dark line that extends across all curves points to the formation of carbides in the material. As the cooling rate ended at approximately 100 °C, the martensite finish Mf region was not recorded. At the bottom of each curve, the measured Vickers hardness values are shown at a load of 5 kg. We can notice that the hardness dropped smoothly with the reduction in the cooling rate of the material. The initial temperature was set at 1030 °C on which the time duration was

always 10 min. to continuously overheat the entire sample throughout the bulk of the material. We can notice that second cooling curve (cooling rate of 5 °C·s^{-1}) passes precisely across the boundary that marks the formation of a bainitic change. The critical cooling rate when the pearlite conversion is to be initiated according to the CCT diagram is determined for a cooling rate of approximately 0.15 °C·s^{-1}. Compared to the metallographic structure in the cooling curve of 0.2 °C·s^{-1}, there was not observed any length change due to pearlite formation in the dilatometric curve. This can be due to overlap of the carbide formation and pearlite formation, as each of these processes influence the length change in the opposite direction. The resulting CCT diagram serves as a starting point for the heat treatment of X153CrMoV12 high-strength tool steel (Fig. 15)

.

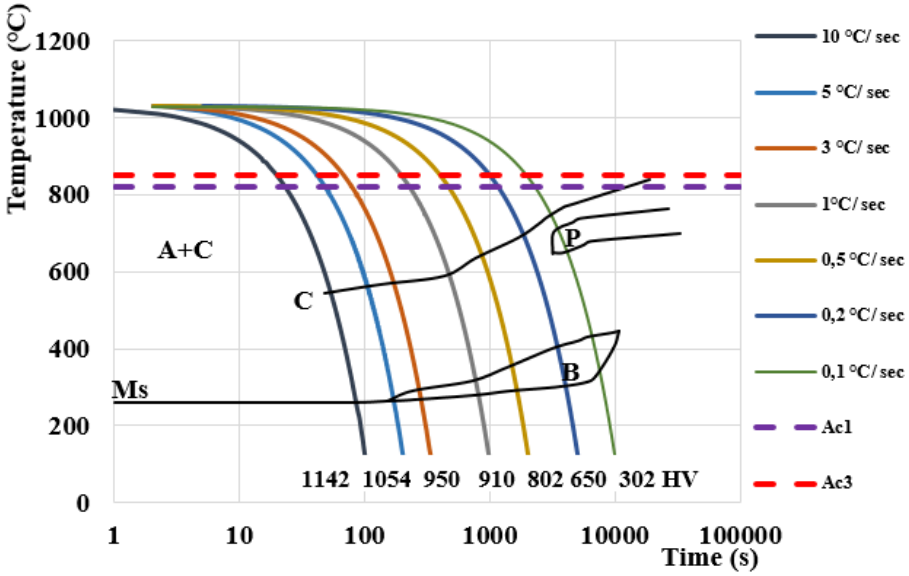

Fig. 15 CCT diagram X153CrMoV12 steel
Source: authors.

5 CONCLUSION

The phase transformation kinetics under continuous cooling conditions was examined in detail using dilatometry, metallographic analysis and nanoindentation hardness test. The results are presented in the form of CCT diagram, which can be useful in designing of the temperature cycles for the production and processing of high performance tool steel X153CrVMo12. The higher percentage of chromium in the material results in the formation of Cr_7C_3 carbide, which results in an increased value of the hardness of the material [9, 10]. Provided the martensitic transformation is achieved, the resulting critical cooling rate is set at 5 °C·s^{-1}. This rate is precisely bordered where literature sources suggests that triple tempering should be followed to achieve the resulting uniform structure of the material. The results of chromium carbides show that at high cooling rates the incidence of hard carbides occur. With decreasing of cooling rates, Fe3C carbides are beginning to occur. Using the AFM microscope, surface topographies of each sample were evaluated to clearly show the sizes of the individual types of carbides as well as their distributions. The resulting sample hardness points to the classic situation where with decreasing cooling rate the hardness of the material decreases and vice versa. The highest hardness achieved value of 1142 HV at the highest cooling rate of 10 °C·s^{-1}. The value of this hardness is mainly affected by the large occurrence of Cr_7C_3 carbides as well as the martensitic matrix.

References

[1] JURČI, P., J. CEJP and J. BRAJER. Metallurgical aspects of laser surface processing of PM Cr-V ledeburitic steel. In: *Advances in Materials, Science and Engineering*. 2011, p. 1-5. ISSN 1687-8434. Available at: https://doi.org/10.1155/2011/563410

[2] PAŠÁK, M., R. ČIČKA, P. BÍLEK, P. JURČI and L. ČAPLOVIČ. Study of phase transformations in Cr-V tool steel. In: *Materiali in Tehnologije*. 2014, **48**(5), p. 693-696. ISSN 1580-2949.

[3] MAN, J., K. OBRTLÍK, C. BLOCHWITZ and J. POLÁK. Atomic force microscopy of surface relief in individual grains of fatigued 316L austenitic stainless steel. In: *Acta Materialia* 2002, **50**(15), p. 3767-3780. ISSN 1359-6454.

Available at: https://doi.org/10.1016/S1359-6454(02)00167-2
[4] MAN, J., B. VALTR, M. WEIDNERC, M. PETRENEC, K. OBRTLÍK and J. POLÁK. AFM study of surface relief evolution in 316L steel fatigued at low and high temperatures. In: *Procedia Engineering*. 2010, **2**(1), p. 1625-1633, ISSN 1877-7058. Available at: https://doi.org/10.1016/j.proeng.2010.03.175
[5] WEI, Y., X. WEI-HONG, L. YA-XIU, B. BING-ZHE and F. HONG-SHENG. Effect of chromium on CCT diagrams of novel air-cooled bainite steels analyzed by neural network. In: *Journal of Iron and Steel Research*. 2007, **14**(4), p. 39-42. ISSN 1006-706X. Available at: https://doi.org/10.1016/S1006-706X(07)60055-7
[6] JIRKOVÁ, H., L. KUČEROVÁ and B. MAŠEK. The Effect of Chromium on Microstructure Development During Q-P Process. In: *Materials today: Proceedings*. 2015, p. 627-630. ISSN 2214-7853. Available at: https://doi.org/10.1016/j.matpr.2015.07.362
[7] SCHINO, A. D. Analysis of phase transformation in high strength low alloyed steels. In: *Metalurgija*. 2017, **54**, p. 349-352. ISSN 0543-5846.
[8] ZRNÍK, J., I. MAMUZIČ and S. V. DOBATKIN. Recent progress in high strength low carbon steels. In: *Metalurgija*. 2006, **45**(4), p. 323-331. ISSN 0543-5846.
[9] KRBAŤA, M., M. ECKERT, D. KRIŽAN, I. BARÉNYI and I. MIKUŠOVA. Hot Deformation process analysis and modelling of X153CrMoV12 steel. In: *Metals*. [online] 2019, **9**(10), p. 1125-1142. Available at: https://doi.org/10.3390/met9101125
[10] BARÉNYI, I., J. MAJERÍK, Z. POKORNÝ and J. SEDLÁK. Material and technological investigation of machined surfaces of the OCHN3MFA steel. In: *Kovové Materiály (Metallic Materials)*. 2019, **57**(2), p. 131-142. ISSN 1338-4252. Available at: https://doi.org/10.4149/km_2019_1_131

Dipl. Eng. Michal **KRBAŤA**, PhD.
Department of Engineering Technologies
and Materials
Faculty of Special Technology
Alexander Dubček University of Trenčín
Ku kyselke 469
911 06 Trenčín
Slovak Republic
E-mail: michal.krbata@tnuni.sk

Dipl. Eng. Róbert **CÍGER**
Department of Engineering Technologies
and Materials
Faculty of Special Technology
Alexander Dubček University of Trenčín
Ku kyselke 469
911 06 Trenčín
Slovak Republic
E-mail: robert.ciger@tnuni.sk

Michal Krbaťa – was born in Trenčín, Slovakia in 1988. He received his Master and PhD. degrees at Alexander Dubček University of Trenčín, Faculty of Special Technology in Trenčín. In his research he focuses on materials research, tribology and dilatometry.

Róbert Cíger – was born in Trenčín, Slovakia in 1996. He received his Master degrees at Alexander Dubček University of Trenčín, Faculty of Special Technology in Trenčín. In his research he focuses on materials research, dilatometry.

DOI: https://doi.org/10.52651/sam.a.2021.1.25-31

STRESS PREDICTION ANALYSIS DURING HOT WORKING OF 100MNCRW4 STEEL

Maroš ECKERT

Abstract: This paper deals with the analysis and the possibility of using a constitutive model based on the Arrhenius equation for tool steel 100MnCrW4. Experimental measurements were performed on a DIL 805 dilatometer in the range of strain rate 0.001 s^{-1} for 10 s^{-1} and temperature from 800 to 1200 °C. Using constitutive equations, material parameters and activation energy were derived, which can be subsequently applied to other models selated to hot behavior of deformation. The experimental data were compared to the ones obtained by the predictive model with the correlation coefficient R = 0.97885 and the parameter MAPE = 17.28 % which means a very good level of prediction.

Keywords: Tool steel; Hot working; True stress; Dilatometry; Arrhenius equation.

1 INTRODUCTION

A constitutive equation or model is a mathematical formulation that establishes a quantitative relationship between two parameters, thereby characterizing material properties. Describes how the material responds to external stimuli and loads. These parameters can be stress - deformation, temperature - heat flow, el. voltage - el. current, etc. depending on the dependencies sought [1, 2]. In the case of forming the material at elevated temperatures, there is a dependence between the actual stress and the deformation. At higher temperatures, various metallurgical and structural changes in the material can occur, which the constitutive equation must capture, and thus its complexity increases. At the same time, it is difficult to create a single model that takes into account all the effects of transformation rate, temperature and other metallurgical phenomena on the course of stress.

In material processing, theoretical constitutive models are used to describe the behavior of materials, taking into account the combined effects of strain hardening, hardening due to transformation rate and thermal softening at different rates and transformation temperatures [3,4]. Understanding the behavior of ductile materials is essential for modeling structural changes and processes. This is the basis for a precise solution of the thermo-mechanical behavior of materials using finite element methods. A suitable model must be able to mathematically characterize the mechanical properties and their reactions over a wide range of loads [5]. In constitutive models, most parameters are determined based on experimentally obtained stress profiles, and therefore such models can relatively accurately predict the hot working behavior of a material [6].

This research attempted to represent thermal deformation of 100MnCrW4 tool steel by formulating a proper constitutive correlation. The thermal compression was tested at different temperatures and strain rates. From the obtained data the dependences between stress and deformation were made, the so-called flow curves. The flow stress was further analyzed based on the test results. A comprehensive constitutive model involving temperature, strain rate, and flow stress was established. Finally, the reliability of the constitutive model was verified.

2 MATERIALS AND METHODS

100MnCrW4 tool steel was used as experimental material. This tool steel is designed for oil hardening with universal use. Alloying elements are manganese, chromium and tungsten. Tools made of this steel have good wear resistance due to the tungsten content, which also contributes to the higher chromium content. Steel shows good hardenability, fine structure and high toughness [7]. Another important feature is the very good dimensional stability after heat treatment. Chemical composition with limit values allowing the relevant standard is given in Tab. 1, basic properties in Tab. 2. The basic microstructure of annealed steel contains fine carbides in a ferritic matrix (Fig. 1) and tempered martensite (dark areas).

Fig. 1 Microstructure of 100MnCrW4 steel
Source: author.

The samples were processed into a dilatometric device in the form of a roller with a diameter of 5 mm and a length of 10 mm. Such samples are inserted horizontally into the working chamber between two ceramic pistons. They are then compressed

at different rates and at different temperatures. The strain rate was set using a dilatometric device and its values were determined based on standard values from practice. In our case, the strain rate was in the range from 0.001 to 10 s^{-1} and the temperature from 800 to 1200 °C.

3 RESULT AND DISCUSSION

It is based on a phenomenological approach using the Arrhenius equation, transformed into a constitutive equation [8], which expresses the actual stress and strain rate at different temperatures using the Z parameter, known as the Zener-Hollomon parameter [9]. This parameter represents the thermally compensated strain rate, which is widely used to characterize the hot work behavior of materials [10]. This model is based on the assumption that the rate of transformation can be expressed in the form of:

$$\dot{\varphi} = AF(\sigma)\exp\left(-\frac{Q}{RT}\right) \tag{1}$$

where Q is the activation energy of the hot working process and R is the gas constant (R = 8.314 $J \cdot mol^{-1} \cdot K^{-1}$)

$$F(\sigma) = \begin{cases} \sigma^s & \alpha\sigma < 0.8 \\ \exp(\beta\sigma) & \alpha\sigma > 1.2 \\ [\sinh(\alpha\sigma)]^n & \text{pre všetky } \sigma \end{cases} \tag{2}$$

where A, s, β, α are material constants. These constants can be determined directly from experimental data obtained from a dilatometric test. These parameters depend on the transformation, so it is necessary to specify them for each strain value. By default, these parameters are determined for true strain values φ from 0.1 to 0.8 in 0.05 increments. The procedure for obtaining the parameters for the individual transformation values is the same, the following is an example procedure for the values of these parameters for the material 100MnCrW4 and the strain φ = 0.2.

For low stresses, the relationship between the stress and the strain rate is expressed by the power function:

$$\dot{\varphi} = B\sigma^s \quad (\text{for } \alpha\sigma < 0.8) \tag{3}$$

and for high stresses an exponential function:

$$\dot{\varphi} = B'\exp(\beta\sigma) \quad (\text{for } \alpha\sigma > 1.2) \tag{4}$$

where B and B´ are material constants independent of the forming temperature. After logarithmization of equations (3) and (4), the equations are obtained:

$$\ln(\sigma) = \frac{1}{s}\ln(\dot{\varphi}) - \frac{1}{s}\ln(B) \tag{5}$$

and

$$\sigma = \frac{1}{\beta}\ln(\dot{\varphi}) - \frac{1}{\beta}\ln(B') \tag{6}$$

Based on equations (5) and (6), it is possible to determine the parameters s as the inverse of the linear regression direction from the graphical dependence $\ln(\sigma)$ vs. $\ln(\dot{\varphi})$ as:

$$s = \left[\frac{\partial \ln\dot{\varphi}}{\partial \ln\sigma}\right]_T \tag{7}$$

and the parameter β similar to the inverse of the linear regression direction from the graphical dependence σ vs. $\ln(\dot{\varphi})$:

$$\beta = \left[\frac{\partial \ln\dot{\varphi}}{\partial \sigma}\right]_T \tag{8}$$

In Fig. 2a shows the course of the functional dependence according to equation (7) for individual temperature.

Tab. 1 Chemical composition of steel 100MnCrW4 (wt.%)

ISO 4957	C	Mn	Si	Cr	W	V
Min.	0,85	1,80	0,10	0,40	0,40	0,05
Max.	0,95	2,20	0,40	0,65	0,70	0,20
Spectral analysis	0,91	1,83	0,32	0,50	0,64	0,18

Source: author.

Tab. 2 Basic mechanical and physical properties of 100MnCrW4 steel [10]

Mechanical and physical properties	Tensile strength (MPa)	Modulus of elasticity (GPa)	Heat conductivity ($W \cdot m^{-1} \cdot K^{-1}$)	Hardness (HV)	Heat capacity ($J \cdot kg^{-1} \cdot K^{-1}$)
Value	> 612	193	33	810	465

Source: author.

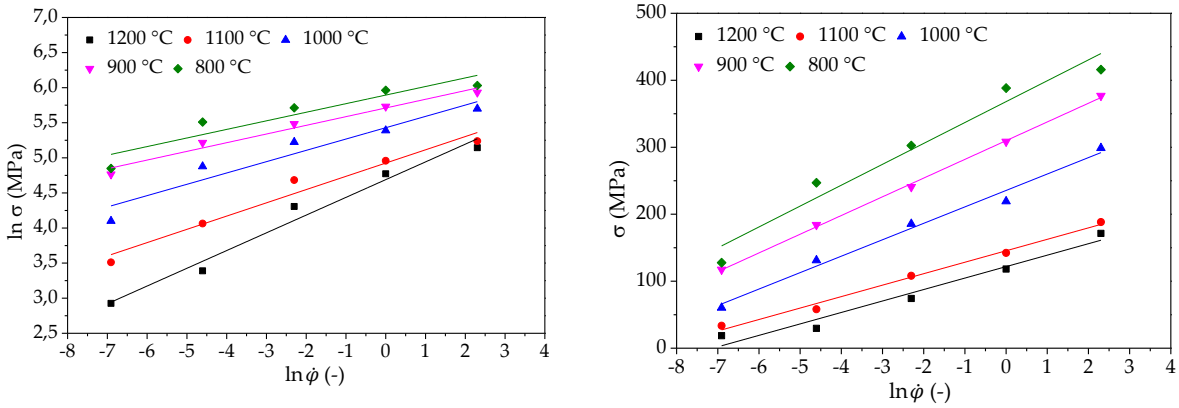

a) b)

Fig. 2 a) Graphical dependence between $\ln(\sigma)$ vs. $\ln(\dot{\varphi})$ to determine the parameter s; b) graphical dependence between σ and $\ln(\dot{\varphi})$ to determine the parameter β
Source: author.

As can be seen, this dependence can be translated by a straight line, and by averaging the inverse value of the directives of the individual straight lines, the value of the parameter s can be obtained. Also in Fig. 2b shows a graphical dependence with the displayed regression lines to determine the parameter β.

For all voltage values (low and high), equation (1) takes the form:

$$\dot{\varphi} = A[\sinh(\alpha\sigma)]^n \exp\left(-\frac{Q}{RT}\right) \tag{9}$$

and logarithmizing it to give the form:

$$\ln[\sinh(\alpha\sigma)] = \frac{\ln\dot{\varphi}}{n} + \frac{Q}{nRT} - \frac{\ln A}{n} \tag{10}$$

Differentiating equation (10) at constant temperature gives the equation:

$$\frac{1}{n} = \left[\frac{\partial \ln[\sinh(\alpha\sigma)]}{\partial \ln(\dot{\varphi})}\right] \tag{11}$$

where the parameter n can again be determined as the inverse average value of the linear regression direction in the graphical dependence between $\ln[\sinh(\alpha\sigma)]$ and $\ln(\dot{\varphi})$ for each forming temperature (Fig. 3a).

According to equation (10), it is possible to create a graphical dependence between $\ln[\sinh(\alpha\sigma)]$ and 1000/T for each transformation speed (Fig. 3b). The value of the linear regression direction in this case is expressed by the values Q/Rn, from which it is possible to express the values of the activation energy Q. From the intersection of the y-coordinate of the dependence between $\ln[\sinh(\alpha\sigma)]$ and $\ln(\dot{\varphi})$ (Fig. 3a) it is possible to determine the parameter lnA according to the equation:

$$\ln A = \frac{Q}{RT} + \frac{C'}{n} \tag{12}$$

where C´ represents the intersection of the y-coordinate by linear regression for each temperature. In this way, the parameters lnA for the respective temperatures are obtained. Subsequently, using equations (9), it is possible to create a model to determine the stresses depending on the transformation rate and the forming temperature using the determined material parameters such as:

$$\sigma = \frac{1}{\alpha}\left\{\left(\frac{\dot{\varphi}\exp\left(\frac{Q}{RT}\right)}{A}\right)^{\frac{1}{n}} + \left[\left(\frac{\dot{\varphi}\exp\left(\frac{Q}{RT}\right)}{A}\right)^{\frac{2}{n}} + 1\right]^{\frac{1}{2}}\right\} \tag{13}$$

In a similar manner, the material parameters are determined for the entire transformation range, which was selected from 0.1 to 0.8 in 0.05 steps. The material parameters depend on the value of the actual deformation and for predicting the voltage in a wide range of temperatures and deformations, the parameters are interpolated by a suitable continuous function. Most often, the obtained parameters are translated by a polynomial function of a certain order [11,12]. The obtained dependences of material parameters were translated by polynomial functions from the 2nd to the 7th degree and the quality of regression was expressed for each degree using the coefficient of determination R^2. The parameter α show sufficient accuracy of the polynomial regression already at the 3rd degree from which the coefficient of determination did not change

significantly (Fig. 4a). The parameters n, Q and lnA achieved sufficient regression accuracy at the 5th degree of the polynomial function (Fig. 4b, c, d).

Then the functions describing the material parameters can be expressed by the equations:

$$\alpha = D_0 + D_1\varphi + D_2\varphi^2 + D_3\varphi^3 \quad (14)$$

$$n = E_0 + E_1\varphi + E_2\varphi^2 + E_3\varphi^3 + E_4\varphi^4 + E_5\varphi^5 \quad (15)$$

$$Q = F_0 + F_1\varphi + F_2\varphi^2 + F_3\varphi^3 + F_4\varphi^4 + F_5\varphi^5 \quad (16)$$

$$\ln A = G_0 + G_1\varphi + G_2\varphi^2 + G_3\varphi^3 + G_4\varphi^4 + G_5\varphi^5 \quad (17)$$

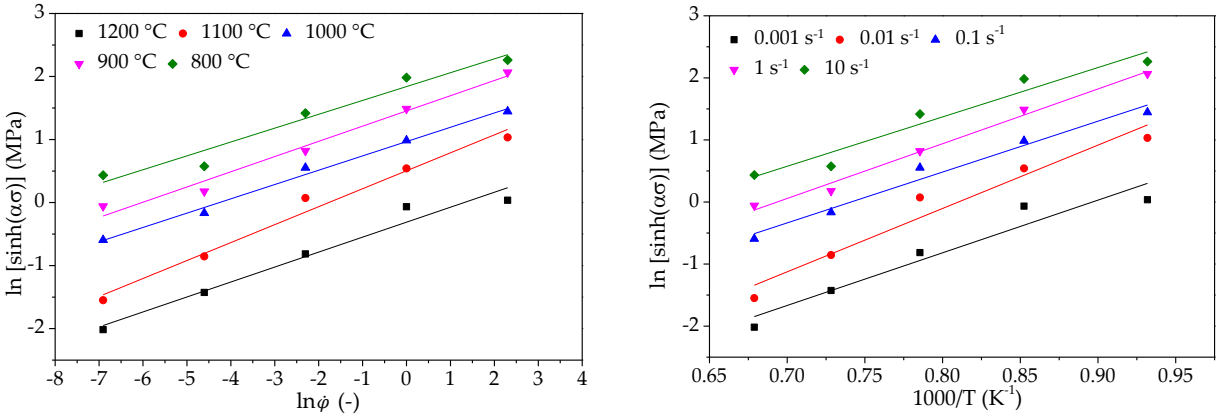

a) b)

Fig. 3 a) Graphical dependence between ln[sinh (ασ)] and ln (φ̇) to determine the parameter n; b) graphical dependence between ln[sinh (ασ)] and 1000/T to determine the parameter Q
Source: author.

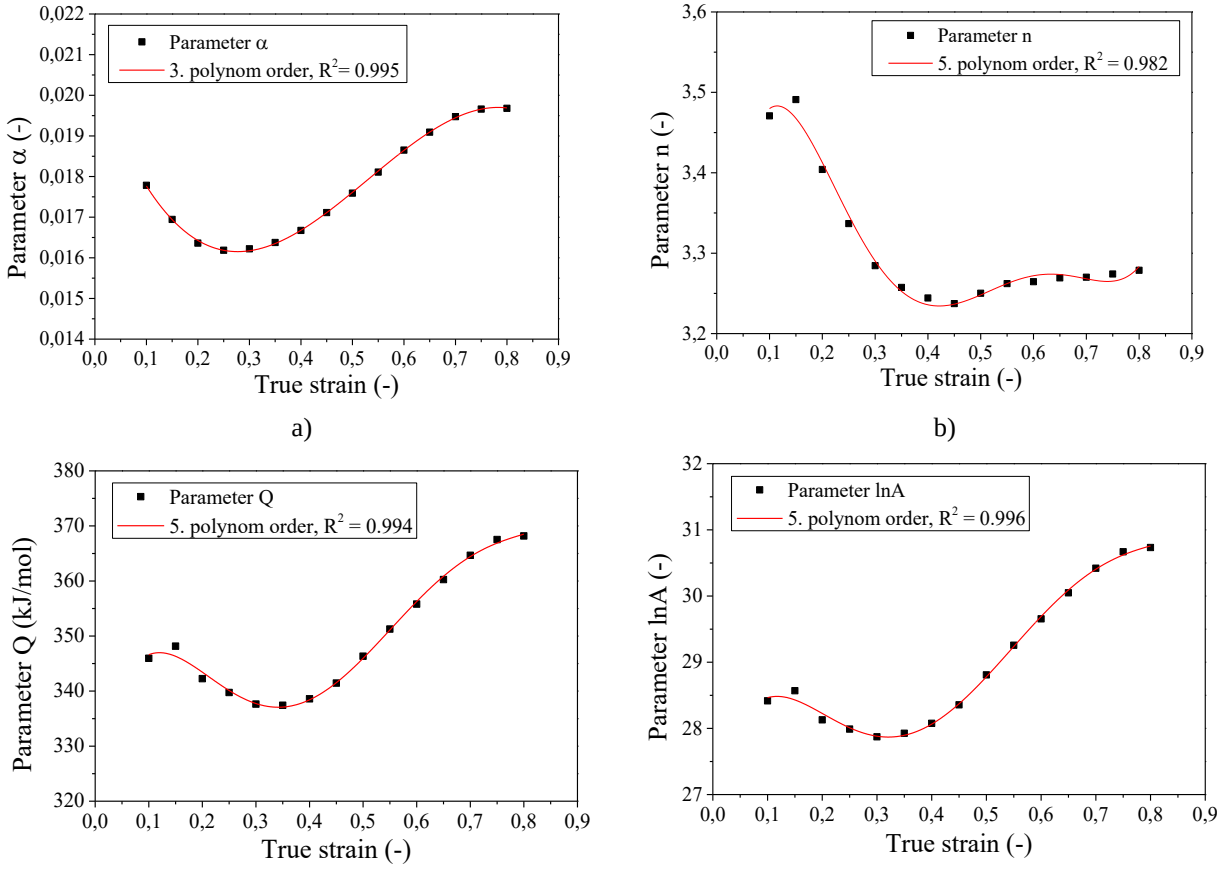

a) b)

c) d)

Fig. 4 Course of material parameters for steel X100MnCrW4 depending on deformation: a) parameter α; b) parameter n; c) parameter Q; d) parameter lnA
Source: author.

Tab. 3 Constants of regression polynomial functions of material parameters for steel 100MnCrW4

Parameter *α* **$F_1(\varepsilon)$**	**Parameter *n*** **$F_2(\varepsilon)$**	**Parameter *Q*** **$F_3(\varepsilon)$**	**Parameter ln *A*** **$F_4(\varepsilon)$**
D_0 = 0,02053	E_0 = 3,1745	F_0 = 326,1688	G_0 = 27,0503
D_1 = -0,03577	E_1 = 6,5989	F_1 = 430,7578	G_1 = 30,3846
D_2 = 0,08734	E_2 = -46,3053	F_2 = -2951,4895	G_2 = -213,4407
D_3 = -0,05492	E_3 = 121,8473	F_3 = 7668,4699	G_3 = 568,5267
-	E_4 = -139,2667	F_4 = -8241,2172	G_4 = -617,4469
-	E_5 = 58,3584	F_5 = 3161,7272	G_5 = 237,4956

Source: author.

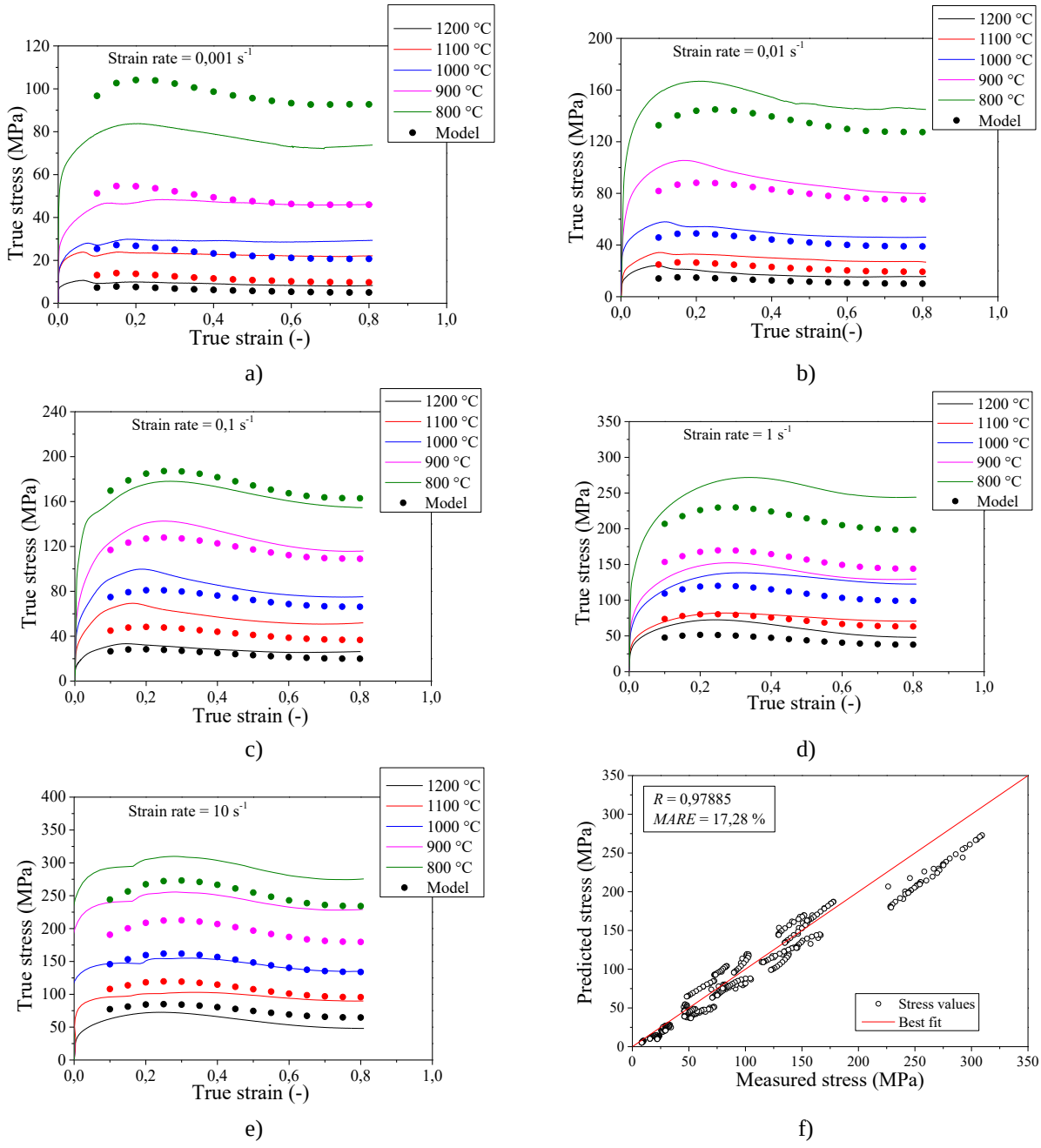

Fig. 5 Comparison between measured and predicted pressure values for 100MnCrW4 material; (a) strain rate $\dot{\varphi}$= 0,001 s^{-1}; b) transformation rate $\dot{\varphi}$= 0.01 s^{-1}; c) transformation rate $\dot{\varphi}$= 0.1 s^{-1}; d) transformation rate $\dot{\varphi}$= 1 s^{-1}; e) transformation rate $\dot{\varphi}$= 10 s^{-1}; f) correlation between predicted and measured pressure values at all transformation rates with expressed correlation coefficient and MAPE

Source: author.

A comparison of experimental and predicted stress values for 100MnCrW4 material is shown in Fig. 5a-e. The course of stresses was created on the basis of equation (13), into which polynomial functions expressing the development of material parameters depending on the transformation were inserted. The values of the constants of the polynomial functions are given in Tab. 3.

Two statistical parameters were used to assess the overall applicability of a given constitutive model. The first was Pearson's correlation coefficient R and the second was the average absolute percentage error of the forecast ("MAPE"). Both parameters were determined from the stress values at all rates and transformation temperatures. Pearson's correlation coefficient is defined as:

$$R = \frac{E\{[\sigma_E - E(\sigma_E)][\sigma_M - E(\sigma_M)]\}}{\delta_x \delta_y} \qquad (18)$$

where E represents the expected value of the actual stress, σ_E and σ_M experimentally and the predicted values of the actual stress, δ_x and δ_y the standard deviations of the stresses. And the MAPE parameter is defined as:

$$MAPE = \frac{1}{n_s}\sum_{i=1}^{n}\left|\frac{\sigma_E - \sigma_M}{\sigma_E}\right| \cdot 100 \qquad (19)$$

where ns represents the number of all stress values. The quality of the prediction based on the value of the MAPE parameter can be determined on the basis of Tab. 4.

Tab. 4 Prediction quality based on the value of the MAPE parameter [13]

MAPE (%)	Prediction quality
< 10	High
10 – 20	Good
20 - 50	Moderate
> 50	Inaccurate

Source: author.

The values of the predicted stresses are in good agreement with the experiments, which is confirmed by the value of the Pearson´s correlation coefficient R = 0.97885 and especially the value of MAPE = 17.28%, which can still be considered a good prediction (Fig. 5f). The largest deviations were achieved at the lowest forming temperature of 800 °C, which means that the given temperature forms the limit temperature for the use of this model for the given steel.

4 CONCLUSION

In this work, hot deformation behaviour of 100MnCrW4 steel was investigated at deformation temperatures from 800 °C to 1200 °C and strain rates from 0.001 s^{-1} to 10 s^{-1}. Constructed flow curves were evaluated using a constitutive model based on the Zener-Hollomon parameters.

100MnCrW4 tool steel exhibits DRX (Dynamic Recrystallization) with a single peak stress in the whole range of temperatures and deformation rates. After reaching the peak stresses, it is possible to observe two predominant courses of flow curves. One is a continuous decrease with a significant DRX mechanism, which occurs especially at lower temperatures (800 °C – 1000 °C) or higher strain rates (1 s^{-1} - 10 s^{-1}) in the entire range of deformation temperatures. The second is only a slight stress drop due to DRX. This course is visible especially at higher temperatures (1200 °C – 1100 °C) and lower strain rates (0.001 s^{-1} – 1 s^{-1}). This is mainly because under these conditions the higher rate of the DRX slows down the strain hardening. This also shifts the peak and steady stresses to lower values of the true strain. Using a constitutive model based on the Arrhenius equation, it is possible to predict the values of flow stresses in a relatively wide range of temperatures and strain rates. The accuracy of the prediction is at the level of the correlation coefficient R = 0,97885 and the parameter MAPE = 17,28 % which means a very good level of prediction.

Acknowledgement

This work was also supported by the Research Agency of the Ministry of Education, Science, Research and Sport of the Slovak Republic under the contract (ITMS2014+) no. 313011W442-CEDITEK II.

References

[1] BAGHERIPOOR, M. and H. BISADI. Effects of rolling parameters on temperature distribution in the hot rolling of aluminum strips. In: *Applied thermal engineering* [online]. 2011, **31**(10), p. 1556-1565. ISSN 1359-4311. Available at: http://dx.doi.org/10.1016%2Fj.applthermaleng.2011.01.005.

[2] SERAJZADEH, S. and Y. MAHMOOD-KHANI. A combined upper bound and finite element model for prediction of velocity and temperature fields during hot rolling process. In: *International journal of mechanical sciences*. 2008, **50**(9), p. 1423-1431. ISSN 0020-7403. Available at: https://doi.org/10.1016/j.ijmecsci.2008.07.004

[3] WANG, X., C. HUANG, B. ZOU, H. LIU, H. ZHU and J. WANG. Dynamic behavior and a modified Johnson-Cook constitutive model of Inconel 718 at high strain rate and elevated temperature. In: *Materials Science & engineering. A Structural materials:*

properties, microstructure and processing. 2013, **580**, p. 385-390. ISSN 0921-5093. Available at: https://doi.org/10.1016/j.msea.2013.05.062.

[4] TAN, Q., M. ZHAN, S. LIU, T. HUANG, J. GUO and YANG, H. A modified Johnson–Cook model for tensile flow behaviors of 7050-T7451 alu-minum alloy at high strain rates. In: *Materials science & engineering. A Structural materials: properties, microstructure and processing*. 2015, **631,** p. 214-219. ISSN 0921-5093. Available at: https://doi.org/10.1016/j.msea.2015.02.010.

[5] LAVAKUMAR, A., S. S. SARANGI, V. CHILLA, D. NARSIMHACHARY, and R. K. RAY. A "new" empirical equation to describe the strain hardening behavior of steels and other metallic materials. In: *Materials science & engineering. A Structural materials: properties microstructure and processing*. 2021, **802,** 140641. ISSN 0921-5093. Available at: https://doi.org/10.1016/j.msea.2020.140641.

[6] HUANG, C.Q., H. DENG, J. P. DIAO and X. H. HU. Numerical simulation of aluminum alloy hot rolling using DEFORM-3D. In: *2011 IEEE International Conference on Computer Science and Automation Engineering* [online]. 2011, **3**, pp. 378-381. Available at: https://doi.org/10.1109/CSAE.2011.5952701.

[7] Available at: https://www.astmsteel.com/product/astm-o1-tool-steel/ [Accessed 8. 3. 2021].

[8] SAMANTARAY, D., S. MANDAL and A. K. BHADURI. A comparative study on Johnson Cook, modified Zerilli–Armstrong and Arrhenius-type constitu-tive models to predict elevated temperature flow behaviour in modified 9Cr–1Mo steel. In*: Computational Materials Science*. 2009, **47**, p. 568-576. ISSN 0927-0256. Available at: https://doi.org/10.1016/j.commatsci.2009.09.025.

[9] ZENER, C. and J. H. HOLLOMON. Effect of Strain Rate Upon Plastic Flow of Steel. In: *Journal of Applied Physics* [online]. 1944, **15,** p. 22-32. ISSN 1089-7550. Available at: https://doi.org/10.1063/1.1707363.

[10] SHANG, X., Y. CUI and M. W. FU. A ductile frac-ture model considering stress state and Zener-Hollomon 368 parameter for hot deformation of metallic materials. In: *International journal of mechanical sciences* [online]. 2018, **144**, p. 800-812. ISSN 0020-7403. Available at: https://doi.org/10.1016/j.ijmecsci.2018.06.030.

[11] WEI, G., X. PENG, A. HADADZEDEH, Y. MAHMOODKHANI, W. XIE, Y. YANG and M. A. WELLS. Constitutive modelling of Mg-9Li-3Al-2Sr-2Y at elevated temperatures. In: *Mechanics of materials* [online]. 2015, **89**, p.241-253. ISSN 0167-6636. Available at: https://doi.org/10.1016/j.mechmat.2015.05.006

[12] LI, J., B. GAO, S. TANG, B. LIU, Y. LIU, Y. WANG and J. WANG. High temperature deformation behavior of 380 carbon-containing FeCoCrNiMn high entropy alloy. In: *Journal of alloys and compounds*. 2018, **747**, p. 571-579. ISSN 0925-8388. Available at: https://doi.org/10.1016/j.jallcom.2018.02.332.

[13] MORENO, J.J.M., A. P. POL, A. S. ABAD and BLASCO, B.C. Using the R-MAPE index as a resistant measure of forecast accuracy. In: *Psicothema Revista de Psicologia*. 2013, **25**(4), p. 500-506. ISSN 0214-9915.

Dipl. Eng. Maroš **ECKERT**, PhD.
Design and Special Technology Department
Faculty of Special Technology
Alexander Dubček University of Trenčín
Ku kyselke 469
911 06 Trenčín
Slovak Republic
E-mail: maros.eckert@tnuni.sk

Maroš Eckert – was born in Ilava, Slovakia in 1989. He received his Master and PhD. degrees at Slovak Technical university, Faculty of Mechanical Engineering in Bratislava. In his research he focuses on materials research, tribology and micro and nanostructural analysis using AFM microscopy.

DOI: https://doi.org/10.52651/sam.a.2021.1.32-42

THE ROLE AND THE RISKS OF EXPLOSIVE ORDNANCE DECONTAMINATION IN HUNGARY

István EMBER

Abstract: The work of the experts of explosive ordnance disposal is very demanding in Hungary. Thousands of explosive remnants of war are still waiting for disarming in the soil. This public duty demands highly trained professionals who are able to meet the requirements of this lethal profession. The statistics are important to receive a complete picture about the background of projectiles and bombs. These military ordnances endanger everybody's live in their close distance. To understand the features of these dangerous devices, first the threats hidden inside their main parts must be identified. This may help us to make the explosive ordnance disposal tasks safer and to understand the possibilities during render safe procedures.

Keywords: Disarming; Decontamination; Explosive ordnance disposal; EOD; Explosives; Threat.

1 INTRODUCTION

The World War II was an enormous concussion for the whole planet. Its effect could also be felt in those countries where there was no factual military action. Our country was not in a good position, because in Europe it was the operational area of the opponent parties for 6 months. Those nations who did not reach Hungary in land warfare, they spread death and devastation in the courses of aerial operations.

These war facts are very determinative, as they have influence on the life of the population after decades. On a daily basis, they have to deal with handling and defusing of explosive ordnances (hereinafter: EO). It is rather impossible to find a construction site in the capital where a sort of grenade or bomb is not to be found. Unfortunately, not just the capital, but also the whole country is implicated. The lethal mechanism present in the entire region is common knowledge, at least for those facing the inconveniences of their handling.

Over the decades, after the end of the World War II hundreds of bomb disposals technicians and explosive ordnance disposals operators (hereinafter: EOD) died a heroic death. This fact confirmed that the threat we face is real, but according to my assumptions, there is a continuously deteriorating presence in the background. Therefore, these explosive devices could be more and more sensitive.

Another important aspect could be analysed by the data related to the alerts. With the analysis of the statistics, we can gain beneficial information, which can help to plan and organise the neutralisation tasks. According to my assumptions, those periods could be identified when the expected number of alerts are rising or decreasing. This could be a good forecast for the bomb disposal tasks.

2 HISTORICAL FACTS

The battles in our country had a great importance. Those military troops, whose main goal was to slow down or stop the Russian frontline, were building barriers, laying minefields on each crossroads, tracks and outskirts of high priority objects. The opponents used the entire spectrum of the military ordnance to reach their operational and strategic goals. [1; 5]

On the former operational areas, millions of artillery projectiles, mortar shells, aerial bombs, hand and rifle grenades, rockets, anti-tank devices, small arms ammunition and landmines were left behind. [2; 19] During the war, the presence of these devices was a serious problem, they could obstruct the different manoeuvres, took lives, but in the period of peace their importance increased. A post-war death is given much more attention since the period of fear is over and people try to step forward. In such a situation it is hard to acknowledge that death is still present and reaps most unexpectedly.

During the Hungarian battles, an amazing number of explosive devices were used, the significant part of which did not explode, the task of their management remaining to posterity. This is a work of professionals, who often give their lives neutralising the explosives. This is not a negligible number: more than 300 professionals died, performing a heroic duty from the end of the World War II until the present day. [2; 155-161] Unfortunately, the number of civilian casualties was significant, and many people lost their limbs or got wounds from shrapnel in the rebuilding period of the country.

3 WHO ARE THE EOD OPERATORS?

We hear many times the term of EOD experts or bomb squad in some news in television or while browsing on the internet. In such a case, we place the associated meaning after the word immediately: Those disarming the bombs. The original meaning of the word was different from the recent one, it formed for decades continuously, until it reached its today content.

The term of EOD operator can be originated from the German "Feuerwerkmesiter". In the beginning, these professionals dealt with the combination and optimisation of the artillery ammunition that remained unexploded as EO. Before World War I,

their main tasks were to take over these projectiles – which are able to explode – from the manufacturers, testing and monitoring them, and destroy those grenades that were not usable. The first cataclysm of the World brought a significant change. The bomb squad also tackled with combat tasks, because grenades and bombs left behind caused a lot of damage to the soldiers; the trained and established bomb patrols' mission was to neutralise the EO that was found. After the war ended, the former system was returned. As the former operational areas fell apart in detached regions of the country, not too many EO have been found; therefore, the expansion of capabilities was not necessary. [2; 13-14]

Later, the increasing number of standardised EO made it necessary that the specialists get serious training. The truly significant development of skill came true in 1939. At that time, neutralising the unexploded aerial bombs was one of the main partial tasks of the air raid precautions; therefore, it was essential to train EOD operators in a rather big number. Until the end of the World War II, hundreds of firemen and civilians got "air raid precaution" EOD training. In 1943, a few trained EOD patrols under the command of the Ministry of Defence were available, who were trained and equipped with modern tools. Their task was the destruction of bombs that were left behind after air strikes. [2; 14-15]

In 1944, an essential thing changed. The fighting arrived in our homeland; thus, the necessity arose for what became an EOD service. The dangerous military ordnance that was left behind and the elimination of the minefields needed much more comprehensive knowledge compared to earlier periods. By this time, not only a few dozen devices had to be prepared for neutralising, but hundreds of different types of explosives.

After World War II, the decontamination of the EO polluted areas had to start. The soviet military engineering units also took their part in these missions, but the millions of ordnance items could be neutralised and overridden only with mobilising huge resources. In Somogy County, the Engineer battalion, which was based there, also took its part in eliminating the minefields. The unit was led by the Bulgarian Major Dimov and Lieutenant Colonel Alajos Fodor. Solving the increased number of neutralisations, they started to use volunteers from the prisoners of war, of course after a quick preparation. These hundreds of volunteers performed a huge task, but they had to pay a dear price for this duty. There was a 10-person demining team, which finished its task with an 80 % human loss. [3; 34-39]

After this period, the engineer units and subunits were continuously reorganised [4], but this did not affect the EOD tasks. The public service mission at this time became crystal clear. The decontamination of the country from the explosive remnants of war seemed to take a long time. In the beginning, the minefields were the main problem; therefore, significant forces were deployed. The minefields were in a continuous area, so this task was not difficult to perform. In such a case, the area to be discharged, sooner or later would be restricted. The case of fired, dropped, or thrown remnants of war is entirely different. It was not possible to localise these types of EO, they could pop up everywhere, as the battle reached the entire part of the country.

As time went by, the specialists also had to face the danger of terrorism. This was separated from the tasks of the Hungarian Defence Forces decades ago, and the EOD unit of the Ministry of the Interior was established. Nowadays, the police department bomb squad is responsible for neutralising the improvised explosive devices. This does not mean that for military experts it is an unknown region, because they have to neutralise the weapons of terrorism across borders, during missions many times, not just in the past but also in the future.

That is the path, which led to the present EOD tasks. It changed a lot since the beginning, but all the time it formed in close relation with the grenades and bombs. The changes always followed the current requirements, and tens of millions of different dangerous materials were neutralised during the past decades. In our days, the amount of newly discovered EO is just a fraction of how many was found during the years after World War II, but it still not negligible. The professionals have thousands of tasks each year, they defuse thousands of remnants of war all over the country. This data itself is extraordinary and predestine the necessity of their public services for many decades to come.

4 STATISTICS REFERRING TO THE EOD TASKS

In the present days, it is no longer necessary to disarm millions of different explosive shells. This is the result of the hard work of the professionals, who risked their lives to clear the minefields and other explosive materials.

However, nowadays it is a significant engagement to deal with deadly assets. Via public service, the soldiers of the Hungarian Defence Forces 1st EOD and Warship Regiment (henceforth: 1st EOD REG) handle thousands of alerts. In order to do this, the 1st EOD REG operates a country wide on-call duty service, where the alerts of suspected explosive devices regularly arrive. This duty works constantly day and night, and it is able to record the received alerts.

Fig. 1 shows alerts for the past 30 years. The variance is very large. The difference between the highest and lowest reporting number is 979, which is a significant difference and shows a 33 % percent decline. Over time, that is an actual declining trend. Compared to an average of 2,379 annual alert number, the number of reported sites has decreased

to around 2,000 in the last four years. This could easily demonstrate a decreasing trend that could be expected. However, this requires further analysis as there have been similar temporary periods in the past.

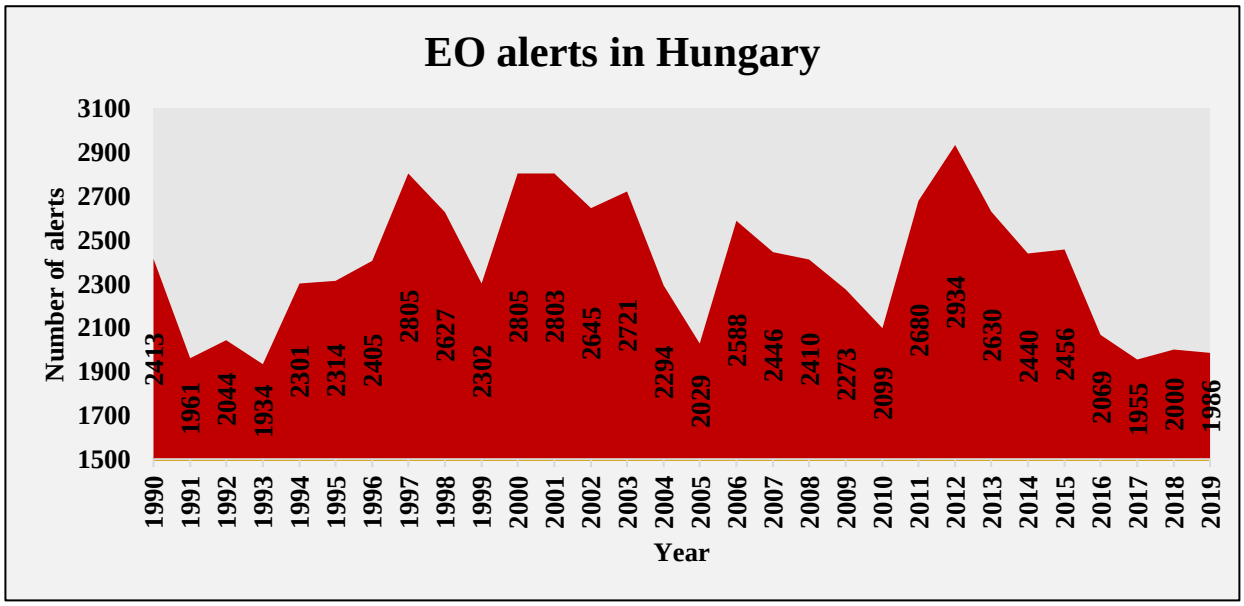

Fig. 1 EO alerts in Hungary
Source: [5].

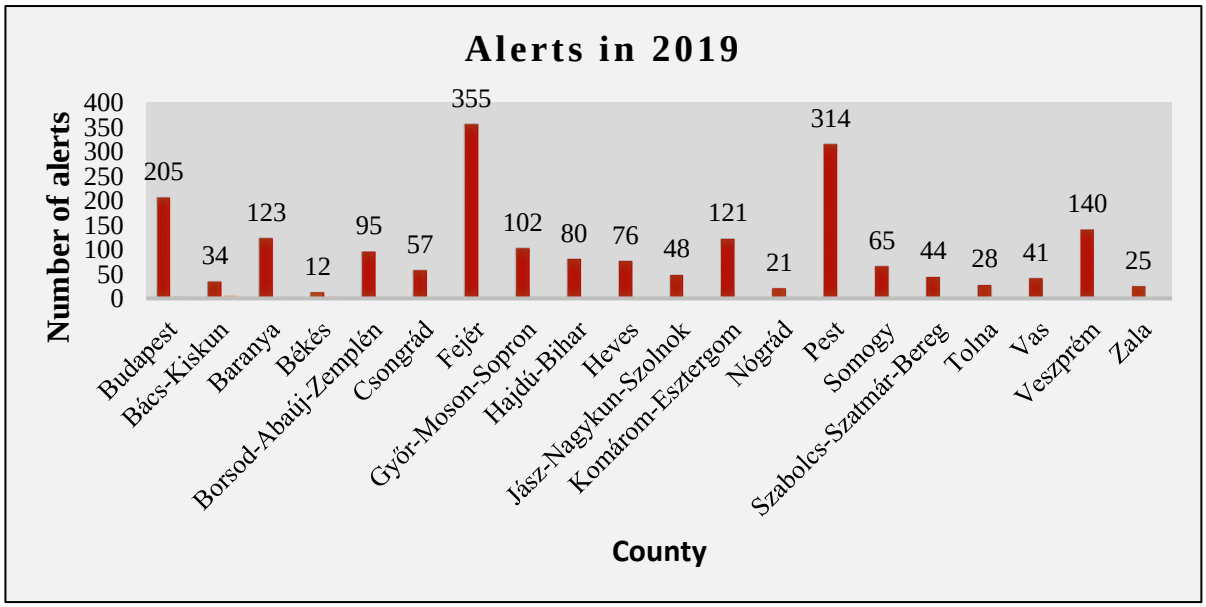

Fig. 2 Alerts in 2019
Source: [5].

In my opinion, several factors affect the annual number of alarms. The trivial aspect is the current state of the construction industry since investments have started with earthworks. Explosive devices may emerge from different depths in the soil, which may be influenced by their mass, material, shape and method of application. In Budapest, it is nearly impossible to build underground parking houses on frequented sites without first disarming air bombs. My personal experience is related to the construction of a garage next to the Parliament, where I had to disarm a Russian FAB-50 demolition bomb (with an AV–1 fuse: all-ways acting, impact detonating type) on 12 January 2014. Similar events happened in 2016 in the 11th district, next to the Rákóczi Bridge. Four air bombs in several meters' depth were found at a relatively small construction area. There were three American GP–1000s among them, and a single German SC–250, but not only these four items were handled by demolition experts on the site. [5]

Examples show that the surrounding areas of World War II priority target buildings and structures can still be contaminated with explosive objects.

Another factor stems from agriculture and forestry. In both areas, there are tasks where tillage is carried out. This work carries the risk of EO being uncovered, especially in areas of major battles. Such areas are along the line of the Danube, Budapest and its surroundings, Győr and its surroundings, Székesfehérvár and its surroundings, and certain parts of the shores of Lake Balaton. [6; 23] A higher number of reports were received from these parts of the country than from the rest. This is well proved by the fact that in 2019, the followings were the most frequented areas in terms of discovered explosive bodies: Fejér County, Veszprém County and Budapest. The dispersion is shown in Fig.2, which also shows that all parts of the country are affected at some level.

The weather should also be taken into account. This may affect several components. In snowy and prolonged winters, relatively less alarms are expected since no explosive objects can be discovered under the snow cover. In this case, hikers do not find suspected explosive bodies and less people spend time outdoors. Rainy, inland water periods and flooding periods also have an impact on the number of reports, as agriculture is pushed into the background. However, extreme drought can significantly increase the number of devices found on the waterfront. In 2018, the Danube River had a very low water level during an extended period. As a result, the number of reports was nineteen times higher for the Danube compared to the number in 2017. In 2018, these reports gave 5 % of the full year reports. [7; 69] It can be seen that extreme weather can also significantly influence the development of statistics.

5 GRENADES AND BOMBS IN HUNGARY

What is the necessary knowledge in the field of EO? Professionals have an enormous knowledge about the hundreds of types of dangerous military ordnance. This huge knowledge is not necessarily enough, and the usage of some databases is a requirement for experts. These sources of information help EOD operators during render safe procedures. The practical classification of EO is the following in Hungary:

- small arms ammunition,
- hand grenades (Fig. 4.),
- rifle grenades (Fig. 5.),
- mortar shells (Fig. 6.),
- anti-tank devices (Fig. 7.),
- artillery projectiles and ammunition (Fig. 8.),
- rockets (Fig. 9.),
- aerial bombs (Fig. 10.),
- landmines (Fig. 11.).

Every type has a different attribute that is well known by the EOD operators. In case of small-arms ammunition, the great majority of non-professionals cannot understand the possible danger in connection with this EO type. Everybody knows these ammunition items, but this familiarity is cursory. They can easily cause lethal wounds. The ammunition on Fig.3 is a 13 millimetres German EO that is quite similar to a 12.7 millimetres machinegun cartridge. Nevertheless, the German one has a fuse and it is filled with explosives, which means it is much more dangerous. It is very important to note that the moving and handling of every ammunition is the job of the highly trained experts.

Fig. 3 13 mm German ammunition
Source: author.

In the class of hand grenades, we can find some subclasses. In general, it can be categorised as an offensive or a defensive type. The defensive type is used thrown from fortified positions because of its high fragmentation effect. The offensive type is used during assault because it has a blast effect with no or minimal fragmentation. There are several other types, too. For example, one of them is used against armoured vehicles. They work with shaped charge by using Munroe effect. According to Gersbeck, the subcategories are the following: fragmentation, blast, heat, bursting smoke, burning smoke, illumination, incendiary, riot control and practice. [8; 116]

Fig.4 Hand grenades (from left to right): Soviet F-1M, German EiHgr–39n. A., Hungarian 42M
Source: author.

"Rifle grenades were devised to cover the tactical range beyond hand grenades. Designs vary from a hand grenade fixed to a simple stabilizer tube assembly to complex designs." [8; 133] The obsolete types were projected with blank ammunition with an additional equipment that was mounted on the rifle. Nowadays, under-barrel grenade launchers are the widespread solutions.

Fig. 5 Rifle grenades (from the top): Soviet VOG–17, German SS G. Pz.gr.–46
Source: author.

Mortars have a large range from 45 millimetres to 280 millimetres. These are filled with explosives or smoke mixture or illuminating mixture or chemicals etc. Mortar shells have a fin that can stabilise their flight but there are some spin stabilised types (these are rare). [9; 2-20] The bigger the diameter is, the bigger the possible destroying effect. The size is not enough because the fuse is important. It has to have a delay function to reach the expected action. These mortar shells are able to annihilate fortified positions. The smaller ones have a fragmentation effect, i.e. they have a point-initiated impact fuse. Between these categories, we can find those mortar shells that are able to operate with both effects. They have a fuse that is point initiated with an adjustable impact action and delay function. It is a rarity, but we can find anti-tank types in the field of mortar shells.

Fig. 6 Mortar shells (from the top): Soviet 82 mm O–832D and O–832
Source: author.

The EO is man-portable in the anti-tank devices category. These devices are developed to destroy armoured vehicles and they are used by the infantry. They have five main parts: warhead, fuse, rocket motor (optional), fin and launcher. For better effects on armoured vehicles, the warheads are designed with shaped charge. They have a rocket motor that is able to improve its effective range. The earlier types were made without a rocket motor; they projected the grenades with gunpowder cartridges or with mechanical solutions. For example, the British Projector Infantry Anti-Tank (PIAT) weapon was made with a powerful spring mechanism. Launcher systems or parts have two variations. The first type is multiple time reloadable; the other type is a single use.

Fig. 7 Anti-tank devices (from the top): German rockets of "Panzerschreck" and "Püppchen"
Source: author.

The projectiles and ammunition used by the artillery is the biggest EO category. This is my opinion based on my experience. We can see the huge variety of calibres, the dozens of subcategories and the thousands of types in this category.

They can be filled with explosives (basic types), chemical agents, riot control chemicals, illuminating mixtures, smoke mixtures, submunitions or propaganda sheets. The basic types have fragmentation, demolition, or combined effect. Projectiles can be stabilised by a spin or fin. Anti-tank projectiles with shaped charge are the most effective when they are fin stabilised. On the other hand, spin stabilised ordnances are more accurate. The fusing can be of impact, time delay or proximity type. Fuses can be in the nose or in the base. [9; 2-17] Sometimes it can be inside-body fuse, like the Hungarian 33M base-placed fuse of a 15 centimetres demolition projectile.

The render safe procedure of artillery projectiles and ammunitions is probably the biggest challenge in Hungary. Maybe this is my personal opinion, but it is based on my executing this demanding task for over 15 years.

Fig. 8 Artillery projectiles and ammunition: Soviet 203 mm projectile G–620, disarmed by the author in 2013, at Székesfehérvár
Source: author.

The rockets category has two main subcategories in the Hungarian practice, these are the unguided rockets and the guided missiles. The unguided rockets are obsolete. They are not so accurate, precise, or high-tech, but these surface-to-surface or air-to-surface devices have a great power that comes from the number of used ordnances at the same time. These rockets are used from multiple rocket launcher systems (e.g. American T–34 Calliope) and rocket pods (e.g. Russian UB–32). "The defining factors that categorize a munition as a "Guided Missile" are that the body being projected:

1. Is propelled by a missile motor or motors. This definition is easier to apply if the motor remains attached to the warhead during flight, but this is not always true.
2. The munition is internally or externally guided and capable of altering its trajectory while in flight." [8; 195]

Fig. 9 Rockets: Soviet M–8 unguided rocket
Source: author.

Types of guided missiles: surface-to-surface, surface-to-air, air-to-surface and air-to-air. Missile sections are the following: guidance section, control section, fin assemblies, motor section, warhead section, fuse section. It can contain some very dangerous parts like high-pressure gas bottles, high-voltage thermal batteries, generators and toxic compounds (e. g. helium bottle in the TOW missile).

The aerial bombs, i.e. the EO that is used by dropping from an aircraft do not meet the definition of rockets (or guided missile). They are attached to an aircraft with one or more lugs, with a few exceptions. For example, the bombs used during World War I were dropped from an open cockpit and they do not have any cleats. [8; 155-167]

1. "High Explosive:
   a) Fragmentation.
   b) General Purpose (GP) old style.
   c) GP new style.
   d) GP demolition bomb.
   e) Penetration.
   f) Guided.
   g) Fuel Air Explosive (FAE).
2. Fire:
   a) Photoflash.
   b) White Phosphorus (WP).
   c) Napalm.
3. Practice:
   a) With explosives or spotting charges.
   b) Inert." [8; 160-161].

Fig. 10 Aerial bombs: U.S. GP-2000, disarmed by the author in 2016 at Budapest
Source: author.

The predecessor of landmines is the so-called "land torpedo". Fedor Zubovics was the person who developed the high-level usage of it. [10; 21] Landmines cause huge problems all over the world. Minefields are armed after a war and the former warring parties have to face the challenge and the cost of demining. It is very important to remove those landmines because they can block the agricultural work, the restart process of the economy and endanger civilians' life. They can be hand or mechanically laid. The laying may occur by vehicles or with a dispenser unit like a submunition.

According to Gersbeck, this is the classification of landmines:

1. "Anti-personnel (APERS or AP).
   a) Blast.
   b) Fragmentation (frag).
   c) Bounding fragmentation.
   d) Directional fragmentation.
2. Anti-tank (AT).
   a) Blast.
   b) Armor-penetrating with shaped-charge or Explosively Formed Projectile (EFP).
3. Practice." [8; 232]

Fig. 11 Landmines: German Tellermine 43 anti-tank mine
Source: author.

The render safe procedures of these military ordnances can cause significant challenges to

professionals. They find obsolete devices on a daily basis, but because of the circumstances, sometimes this is much more problematic, than the disarming of modern ordnances. Every type of EO present in Hungary is shown here in my article. We can see on Tab. 1 the number of devices that are identified all over Hungary. It is easy to see that the number of small arms ammunition is the biggest, but the categories of artillery projectiles, ammunition and mortar shells are the most relevant. The numbers are not so important in these last two categories due to the size of the EO. For example, 1 piece of Russian 203 mm artillery projectile (Fig. 8) which has a demolition effect (type code: G–620, also called concrete-buster projectile) weights more than 100 kilograms. The most common disarmed EO in Hungary (based on my experience) is the Russian 82 millimetres mortar shell (Fig. 6) which has a fragmentation effect (type code: O–832 or O–832D). There is a contracted category in the table below for the other military devices like rifle grenades, rockets, fuses, parts of ordnances etc. I would like to underline the status of landmines in Hungary. The experts do not have to disarm a lot of them, because of the demining operations after the World War II.

The current status shows us that the EO clearance process is far from being finished in Hungary. The number of disarmed dangerous military devices verifies the importance of the public duty of EO experts. The outstanding numbers and the state of unarmed devices show the real volume of this task.

Now we can see the extreme danger behind this job, and we can understand the deep vocation necessary to pursue this profession.

Tab. 1 Number of identified EO from 2015 to 2019

No.	Name	2015	2016	2017	2018	2019
1.	Number of alerts	2,456	2,069	1,955	2,000	1,986
2.	High priority alerts	638	525	526	526	444
3.	Small arms ammunition	8,974	5,965	34,333	28,526	27,931
4.	Hand grenades	369	294	423	470	364
5.	Mortar shells	692	863	869	893	747
6.	Artillery projectiles and ammunition	4,585	3,708	1,221	3,575	2,486
7.	Aerial bombs	1,060	361	361	158	386
8.	Landmines	14	18	16	7	16
9.	Other unexploded ordnances	4,454	1,432	4,270	2,437	2,838
10.	Other safe objects (Did not contain any explosive or pyrotechnical parts).	801	742	552	2,506	3,476
11.	**Total**	**20,148**	**12,641**	**41,493**	**36,066**	**34,768**

Source: [5].

6 EO DANGEROUS FEATURES

Now we can see the enormous number of the possible EO alerts. EOD operators have to handle every alert as quickly as possible, but it is very demanding because of the number and type of grenades, bombs, landmines and projectiles. It is also hard to disarm the ordnances because of their large number: a few ten thousand pieces on a yearly basis in Hungary. After this, the sources of danger coming from the EO have to be examined. A non-professional may think that time works against these dangerous devices. They think that the aerial bombs, projectiles, and landmines become unarmed because of the natural degradation of explosives. Sometimes it happens, but there is the possibility of the worsening safety condition of explosives. Thus, it is very important to define those factors that have any influence on the render safe procedures.

6.1 The Explosive Charge

The process inside an EO is identical to explosive trains working. “In other words, the initiator, containing mainly primary explosive, is initiated by a small energy input and its explosive output initiates

the booster, which in turn, initiates the main charge that is, HE filling. The booster is sufficiently insensitive yet capable of initiation by the initiator. Booster explosives are limited in number (Tetryl and PETN) and their explosive properties are in between initiators and main charges." [11; 39]

The great majority of EO items are made and designed to annihilate troops, technical equipment, vehicles and buildings. Generally, this destroying power is coming from the main charge that is inside its body. Naturally, there are some exceptions. These ordnances do not contain explosive or main charge. Without any explosive materials, these projectiles are not authoritative, and I will not analyse them.

Almost every time, the blast of EO is a condensed-phase explosion. We can find a few exceptions. Some aerial bombs use liquid fuel. This type of bomb can create a fuel cloud in the air that is able to explode. These bombs are also called thermobaric bombs, vacuum bombs, or aerosol bombs.

Generally, the explosion is a very quick chemical transformation and this process generates a lot of energy. This energy or demolition power comes from the gases of chemical transformation. The gases rise and spread in the air and they have a high pressure, high velocity and high temperature. [10; 20]

The military EO are filled with military explosives. This is a very important point, because these explosives are much more reliable and stable than their industrial versions. Sometimes it is problematic to reach higher quality in a factory in wartime. In such a case, the production quantity is maximised, and the explosives can have an inferior quality. This is not an enormous problem, when there is a short time between production and usage. The usage is rather quick in wartime. On the other hand, the unexploded ordnances under the ground and the stockpiled ammunition can be problematic due to impure explosives. These polluted materials can be the fertile ground of a chemical transformation or recrystallisation.

"TNT, RDX and HMX are typical crystalline material used for explosive." [12; 77] These materials are not just explosives, these are military grade explosives. I will therefore analyse TNT (trinitrotoluene or trinitrotoluol or trotyl) to illustrate this problem. It is a widespread military use, secondary explosive. "TNT is still the most important explosive for blasting charges of all weapons. It is very stable, neutral, and does not attack metals; it can be charged by casting as well by pressing; it is insensitive and needs no phlegmatizers. It can be applied pure and mixed with ammonium nitrate (Amatols), aluminium powder (Tritonal), with RDX (Composition B), and combinations (Torpex, HBX, Trialenes)". [13; 338]

This perfect material is able to produce some awkward chemical processes. According to Meyer, Köhler and Homburg, TNT does not attack metals, but Orlova's book shows us another viewpoint. A Meisenheimer complex can arise from TNT in the presence of an alkaline solution and the metal salts of toluene can reach the sensitivity of primary explosives. [14; 89]

What does it mean in practice? The EOD operators have to handle those military ordnances that were fired or dropped. These grenades and bombs were exposed to extreme energy during their launch and when they hit their targets. This is not enough. Sometimes these military ordnances were also exposed to bad weather conditions for seven decades. The extreme energy could cause damage to the main charge, which means that the main charge could crack or/and compact. The cracks provide the chance for the effects of weather to reach the explosive charge. A damage inside the main charge can result in the appearance of air gaps that are necessary for the crystallisation process.

In the case of TNT, there is also a possible problem during the storage time. If the explosive has a bad quality (it is polluted with bad isomers), the so-called "toluene oil" separates from it. [14; 93] This separation can cause volume reduction and the explosive diverges from the wall of the charge cavity, the varnish layer can exfoliate and air gaps arise. The space inside the explosive charge is conducive to the crystallisation process and bigger crystals may grow, which is a very dangerous condition. It is prohibited to use an EO like this because of accidental explosion. These military ordnances will not be able to handle the force effect of launch or fire and only EO operators are eligible to move or disarm them. In this situation, the EO operator has to choose a nearby blasting area that is proper to annihilate them.

Concerning the danger of explosives, there is also another viewpoint. For example, TNT is toxic, and it is able to poison the human body through skin. It can attack the hematopoietic system and the digestive system. [14; 92] It can also destroy nature through its toxicity. Because of these toxic explosives, the wildlife is in real danger, but not every race is equally vulnerable. [15; 171] The explosives start to degrade in nature. The photochemical degradation changes its colour from yellow to brown. Bacteria of soil are able to degrade TNT and other dangerous materials. [16] Fungal degradation is also possible. [17] It does not mean that bacteria and fungi can disarm unexploded ordnances under the ground, because they cannot get into the ordnances.

6.2 Fuses

The fuses of the EO provide for the explosion to happen at the right time and in the right place. These devices can be simple and expressly complex. The simplest type works like a cartridge cap without any mechanical parts. There are several types, which use the blending of chemical components or a chemical method is used during the arming process. A cutting-edge equipment is built up with electronic parts like

Global Position System, Infrared System, and Proximity Sensor System etc. I will not analyse these modern devices, because EO troops never disarm fuses like these during public duty in Hungary. [18; 208-210]

In order to demonstrate the risks caused by an EO fuse, I show a British one. The No. 17 Mk I, II, III bomb fuse (Fig.12) is one of the most dangerous devices. This is a tail fuse or pistol with a chemical delay of half an hour to 36 hours. The basic principles of operation are impact (mechanical) action, chemical action and anti-withdrawal action. The arming mechanism works through the vane. The arming time lasts until the vane finishes eight spins. It is used in several types of aerial bombs (GP 250 Mk I, II, III and GP 500 Mk I, II, III, V). [18; 208-210]

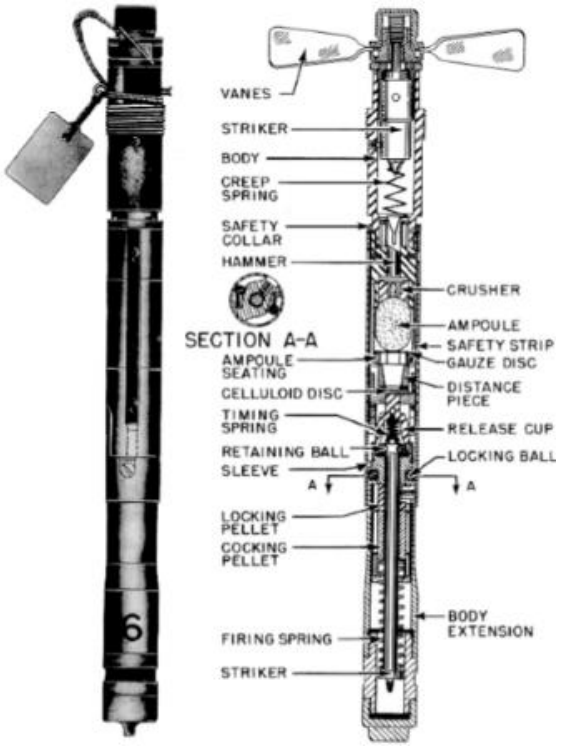

Fig. 12 British aerial bomb fuse No. 17
Source: [18].

The most important parts of the operation of the fuse are the followings: after the arming process, when the bomb hits its target and the striker weight (through the hammer and the crusher) smashes the ampoule which is filled with acetone, after a few other processes the acetone corrodes the delay celluloid disc, when the celluloid disc is softened or dissolved the timing spring lifts up the release cap and the cocked firing spring can force (retaining balls are also forced to move out of the way) the striker to hit the detonator's cap.

We can find some very important information in the last example. The explosion of the bomb depends on a small celluloid disc inside the fuse. This celluloid part is durable, but we cannot know the extent of the action of the acetone. It might happen that the disc is only partly dissolved during the arming process. Later, the bacteria and the bad effects of weather could worsen this condition due to damaged parts. This is a very hard situation for an EOD team, because they do not know the actual state or stability of the fuse. Furthermore, it is impossible to unscrew the fuse, because it has an anti-withdrawal action.

The render safe procedure of these devices is one of the greatest challenges. It can show us clearly that the fuses are very dangerous parts of an EO despite the fact that they spent 70 years in the soil. Not every ordnance is so problematic like this, but one type is enough to set up a new rule or a new disarming process in this profession.

6.3 Other sources of danger

Nowadays, the number of terrorist attacks committed with explosions is increasing, and it is widespread all over the world. [19; 258-259] I will not analyse the risks of the improvised explosive devices (Victim Operated, Time Delay, Suicide Born, Radio Controlled etc. [20]) and the homemade explosives, because this is the duty of the Hungarian Police.

I would also like to avoid the Chemical, Biological Radiological and Nuclear EOD tasks in this article, because this field of disarming is very complex. This task demands specially and highly trained troops. [21; 25] Thus, I accept the fact that these ordnances are very hazardous.

7 CONCLUSION

Now we can see a general idea about the quantity of the tasks of EOD teams in Hungary. The number of alerts and the statistics of the last few years forecast a very long term when the professionals will have to handle dangerous remnants of war on a daily basis. The number of identified EO is high, and the organising of the render safe procedures demands high prudence.

I identified a few sources of danger during the review of EO. These devices may cause lethal danger after more than 70 years. Besides, they are able to cause more highly dangerous conditions than ever before. The possible chemical transformation of explosives and the corrosion or deformation of the inner parts of fuses makes the unarming process much riskier. The handling of a CBRN EO is an extremely challenging task and the worsening processes make it more and more dangerous.

Data and processes show us the world of EOD operators. This world is full of challenges and danger and only the most dedicated troops have the right to pursue this profession.

Acknowledgement

This study was sponsored by the National University of Public Service in Hungary, during the framework of the "2019. évi Tématerületi Kiválósági Program" research project.

References

[1] GELLÉRT, T. *Tűz és víz katonái. MH 1. Honvéd Tűzszerész és Hadihajós Zászlóalj*. Budapest: Zrínyi Katonai Kiadó, 1981.

[2] BUCSÁK, M., A. CSURGÓ, T. HORVÁTH, L. LÁNG, S. MOLNÁR, L. POSTA, ZS. SZATAI and VÖRÖS, M. *70 év az életveszély árnyékában. A magyar tűzszerész- és aknakutató alakulatok története 1945–2015*. Budapest: Zrínyi Kiadó, 2015. ISBN 9789633276532.

[3] FEHÉR, J. Akna és lőszermentesítés Somogyban. In: HAJDU, R. J., PAP, J. (eds.) *Aknászok, tűzszerészek. Hős magyar honvédek a II. világháborúban és a következő években.* Mezőkövesd: Legatum, 2006. ISBN 9638722606.

[4] KOVÁCS, T., J. NYERS and J. PADÁNYI. *Építünk, védünk, alkotunk. A műszaki csapatok története 1945-től napjainkig.* Budapest: Zrínyi Kiadó, 2012. ISBN 9789633275412.

[5] Compiled by the author based on the HDF 1st EOD REG's archive.

[6] VÖRÖS, M. and DARUKA, N. Tűzszerészek a közszolgálati feladatok ellátásában. In: *Seregszemle*. Székesfehérvár: *MH ÖHP* [online]. 2012. **10**(2), pp. 22–33. [cit. 2020-03-05]. Available at: https://honvedelem.hu/files/files/33676/seregszemle_2012_2.pdf

[7] EMBER, I. A dunai alacsony vízállások tűzszerész tapasztalatai 2018-ban. In: *Műszaki Katonai Közlöny* [online]. Budapest: Ludovika Egyetemi Kiadó, 2019. **29**(3), pp. 65–78. ISSN 2063-4986. [cit. 2021-02-25]. Available at: https://doi.org/10.32562/mkk.2019.3.5

[8] GERSBECK, T. *Practical Military Ordnance Identification*. Boca Raton: CRC Press, 2014. ISBN 9781439850596. Available at: https://doi.org/10.1201/b16615

[9] DEPARTMENT OF THE ARMY – U.S. MARINE CORPS: *Unexploded Ordnance (UXO) Procedures (FM 21-16).* [online] Washington, D.C.: Department of the Army, 1994. [cit. 2021-02-25]. Available at: www.globalsecurity.org/military/library/policy/army/fm/21-16/index.html

[10] LUKÁCS, L. *Szemelvények a magyar robbantástechnika fejlődéstörténetéből.Különös tekintettel a továbbfejlesztés várható irányaira és a kor új kihívásaira*. Budapest: Dialóg Campus Kiadó, 2017. ISBN 9786155680359.

[11] AGRAWAL, J. P. *High Energy Materials*. Weinheim: Wiley-VCH, 2010. ISBN 9783527326105. Available at: https://doi.org/10.1002/9783527628803

[12] KUBOTA, N. *Propellants and Explosives – Thermochemical Aspects of Combustion*. Weinheim: Wiley-VCH, 2002. ISBN 3527600507. Available at: https://doi.org/10.1002/3527600507

[13] MEYER, R., J. KÖHLER and A. HOMBURG. *Explosives*. Weinheim: Wiley-VCH, 2007. ISBN 978-80-527-31656-4.

[14] ORLOVA, J. J. *Brizáns robbanóanyagok kémiája és technológiája*. Budapest: Műszaki Könyvkiadó, 1986. ISBN 9631064662.

[15] JOHNSON, M. S. and C. J. SALICE. Toxicity of Energetic Compounds to Wildlife Species. In: SUNAHARA, G. I., G. LOTUFO, R. G. KUPERMAN and J. HAWARI. (eds.) *Ecotoxicology of Explosives*. Boca Raton: CRC Press, 2009. ISBN 9780849328398.

[16] AHMAD, F. and J. B. HUGHES, J. B. Anaerobic Transformation of TNT by Clostridium. In: SPAIN, J. C., J. B. HUGHES and H. KNACKMUSS. (eds.) *Biodegradation of Nitroaromatic Compounds and Explosives*. Boca Raton: CRC Press, 2000. ISBN 1566705223.

[17] FRITSCHE, W., K. SCHEIBNER, A. HERRE and M. HOFRICHTER. Fungal Degradation of Explosives: TNT and Related Nitroaromatic Compounds. In: SPAIN, J. C., J. B. HUGHES, and H. KNACKMUSS. (eds.) *Biodegradation of Nitroaromatic Compounds and Explosives*. Boca Raton: CRC Press, 2000. ISBN 1566705223. Available at: https://doi.org/10.1201/9781420032673

[18] DEPARTMENT OF THE NAVY, ORDNANCE SYSTEMS COMMAND: *British EO*. s. l. Naval Ordnance System Command, 1946.

[19] HORVÁTH, T. A műveleti környezet műszaki támogatásának kihívásai. In: KRAJNC, Z. and J. CSENGERI. (eds.) *Humánvédelem – békeműveleti és veszélyhelyzet-kezelési eljárások fejlesztése* [online]. Budapest: Nemzeti Közszolgálati Egyetem, 2016. [cit. 2020-03-29]. Available at: http://real.mtak.hu/33554/1/tanulmanygyujtemeny%20_ujratervezes_CsJ_KZ_1.5.pdf

[20] KOVÁCS, Z. Az improvizált robbanóeszközök főbb típusai. In: *Műszaki Katonai Közlöny* [online]. Budapest: NKE HHK és MHTT Műszaki Szakosztály, 2012. **22**(2), pp 37–52. ISSN 2063-4986 [cit. 2020-03-29]. Available at: https://mkk.uni-nke.hu/document/mkk-uni-nke-hu/2012_2_03_IED-k_főbb_típusai_-_Kovács_Z.pdf

[21] BEREK, T. ABV (CBRN) tűzszerészcsoport, mint a biztonsági kihívásokra adott válaszlépés. In: *Bolyai Szemle* [online]. Budapest: Dialóg Campus Kiadó, 2016. **25**(4), pp. 22–34. [cit. 2021-02-25]. ISSN 14161443. Available at: https://nkerepo.uni-nke.hu/xmlui/bitstream/handle/123456789/14564/ABV%20(CBRN)_%20t%20zszer%C3%A9szcsoport,%20mint%20a%20biztons%C3%A1gi%20kih%C3%ADv%C3%A1sokra%20adott%20v%C3%A1laszl%C3%A9p%C3%A9s.pdf?sequence=1

István **EMBER**, assistant lecturer
Department of Operations and Support
Faculty of Military Science and Officer Training
National University of Public Service
Hungaria krt. 9-11.
1101 Budapest
Hungary
E-mail: Ember.Istvan@uni-nke.hu

István **EMBER** has received two BSc degrees in civilian engineering (2005) and explosive engineering (postgraduate programme in 2016), but he has got also an MSC degree in military leadership. He had been working as an explosive ordnance disposal officer (1st class EOD expert) for 15 years before he started his PhD study in 2019. His main research is related to the actual challenges of EOD support. Furthermore, he is a licenced civilian blasting expert and a pyrotechnician.

DOI: https://doi.org/10.52651/sam.a.2021.1.43-48

PERFORMANCE CHARACTERISTICS OF STEEL 1.2842 AFTER NITRIDATION

Michal KRBAŤA, Jana ESCHEROVÁ

Abstract: The paper deals with the change in mechanical properties and wear of 1.2842 universal tool steel after plasma nitriding, which is widely used to produce cutting tools with good durability and low operating costs. Plasma nitriding was performed at a temperature of 500 °C for 10-hour period in a standard N_2 /H_2 atmosphere with 1:3 gases ratio. Microstructure, phase structure, thickness of a nitriding layer and surface roughness of samples were measured with optical microscopes and a profilometer. Verification of a chemical composition was carried out on the BAS TASMAN Q4 device. Wear resistance was measured on a universal TRIBOLAB UTM 3 tribometer, through a, "pin on disc" method. The results of experiments have shown that plasma nitriding process, significantly improves the mechanical and tribological properties of selected materials.

Keywords: Plasma nitriding; Microhardness; Coefficient of friction; Pin on disc.

1 INTRODUCTION

The 1.2842 tool steel is suitable for the plasma nitriding process due to its chemical composition. This steel has a wide range of applications for the production of universal cutting tools. Authors Studený et al. [1] solved importance of diffusion process on the fatigue life of this type of steel in their scientific research. Investigations with the same workpiece material were also realized by the authors [9,10,12]. Authors Pilch et al. [2] solved the corrosion resistance of turbocharger stator after plasma nitriding process. The authors [4, 5] also studied and dealt with the same problem of plasma nitriding. Tribology of these parts plays an important role in their functionality and lifetime. Tribological problems can often be solved with a surface finish. Authors Doan et al. [3] have dealt with their research with the improvement of wear resistance for C45 steel using plasma nitriding, nitrocarburizing and nitriding. Other authors, such as Dubovská and Majerík [7] conducted the research analysis of surface finish and wear on the special tribological device. The effect of nitrogen on surface morphology of layers was solved by Pokorný et al. [6]. Plasma nitriding, with regard to many advantages unlike common kinds of nitriding, found an increasing industrial application [5, 11]. The main problem of nitridations in salt bathes is connected with toxicity of cyanide salts. Traditional gaseous nitriding requires a longer time for treatment to obtain a needed nitridation depth. Direct current of plasma nitriding (DCPN) has been recently one of the conventional treatments of a surface finish being used in the industry aiming to improve mechanical features and wear resistance of mechanical engineering materials. Various layers may rise on a surface due to plasma nitriding. These layers are classified by composition of particular phases. With respect to the steel composition, its layer is mainly composed of ferrous nitrides (γ'-Fe_4N or ε-Fe_2-3N) and nitrides of alloying elements. Research studies showed that the microstructure of nitriding layer can be affected with change of parameters of nitriding process, as temperature, time and plasma composition of the gas. Changes in microstructure of nitriding layer effect mechanical and tribological features of the material, such as surface hardness, wear resistance and endurance strength [2, 4, 8]. For a diffusion controlled growth, thickness of nitriding layer increases with temperature and nitridation time [6]. However, maximum surface hardness is achieved only at a certain nitridation time and temperature. Previous studies showed that a chemical potential of nitrogen is important in plasma nitriding of steels. The aim of the present paper is to map the effect of plasma nitriding on the resulting values of the coefficient of friction and wear.

2 EXPERIMENTAL MATERIALS

The samples were annealed. The process of plasma nitriding was carried out using the Rubig 60/60 device. The parameters of plasma nitriding were chosen so that nitriding layer is as thick and as hard as possible, (Tab. 1).

Thermally treated and surface finished steel samples were numerically marked. Chemical composition of given steel was verified through a BAS TASMAN Q4 device and subsequently it was compared with the DIN 90MnCrV8 technical standard (Tab. 2).

Measurements of micro hardness and thickness of a nitriding diffusion layer were taken on each sample using the Vickers method. Impressing of a diamond pyramid under vertex angle of 136º is essential to the method. The LECO M400H microhardnessmeter will be used to verify and compare achieved results before and after plasma nitriding. The load force will be 0.5 N and force action time in accordance with DIN 50190 standard will be 10 sec. The measurements of micro hardness will be taken on a cross-section of a nitrided sample, upright from the surface to the material core. The achieved values of hardness will be displayed as a function of distance from a surface. Thickness of a nitride layer will be taken on 18 imprints and 5 imprints in the material core. Limit value in terms of this standard is hardness value, designated as limit hardness GH) and is indicated as

the Vickers hardness and it applies: GH = average measured value in a core + 50 HV (rounded to 10HV).

Metallographic analysis is based on the polishing of samples and a subsequent etching with Nital. Etching of samples brings up their microstructures. We make out matallographical pictures of all samples with the Olympus GX51 optical matallographical microscope. With the microscope we can monitor a size of a white layer as well as an approximated size of a diffusion layer. Then we can assess a resulting structure of a diffusion layer as well as a basic material.

Tab. 1 The parameters of plasma nitriding

Pressure [mbar]	2.8
Voltage [V]	700
Atmosphere PN [N_2 / H_2]	1/3
Temperature PN [°C]	500
Time PN [hour]	10

Source: authors.

Tab. 2 Chemical composition 1.2842 steel [in wt. %]

Element	DIN standard	BAS Tasman Q4
C	0.27 – 0.34	0.34
Mn	0.40 – 0.70	0.69
Si	Max 0.40	0.39
Cr	2.30 – 2.70	2.38
Mo	0.15 – 0.25	0.21
V	0.10 – 0.20	0.20

Source: authors.

Tab. 3 Measurement parameters for tribology

Sample	Heat treatment	Turning radius	Load [N]	Rotation speed [rpm]
1	Annealed	19	50	250
		21	50	
		23	50	
2	Annealed	19	100	250
		21	100	
		23	100	
3	Annealed	19	150	250
		21	150	
		23	150	
4	Plasma nitriding	19	50	250
		21	50	
		23	50	
5	Plasma nitriding	19	100	250
		21	100	
		23	100	
6	Plasma nitriding	19	150	250
		21	150	
		23	150	

Source: authors.

Roughness of surface was measured on the Talisurf CCI Lite 3D device. All samples had been grinded on a mag-netic grinder with 0.001mm precision before plasma nitriding and marking. Surface roughness was measured before and after plasma nitriding aiming to define changes of roughness.

Measurement of wear was executed on the BRUKER UTM 3 device using „pin of disc“ method. This method is based on imprinting a firmly gripped body in a ball shape into a testing material in a disc shape, being rotated with constant revolutions. The testing ball was made of the 440C stainless steel with a 6.35 mm diameter and 746 HV hardness. The measurements were taken from 6 samples at 3 loads and three measurement radiuses. The Measurement radiuses for each sample are shown in (Tab. 3).

3 RESULTS AND DISCUSION

Microstructure of the 1.2842 steel can be seen in Fig. 1, in a treated condition and after having etched 2 % Nital and it was assessed as a perlite and secondary cement. Perlite occurs both in lamellar and globular form. An average micro hardness had a value of 270 HV.

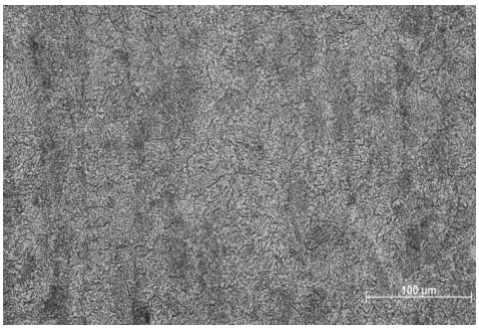

Fig. 1 Cross-sectional microstructure
Source: authors.

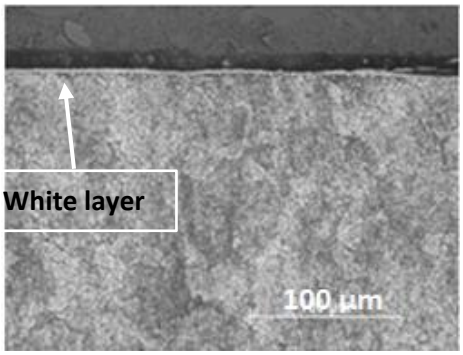

Fig. 2 Cross-sectional microstructure with white layer
Source: authors.

Only thicknesses of white layers were expressly visible and measurable after plasma nitriding on a metallographic section. There is a coherent and relatively white layer of nitrides on the samples surface. Under a white layer there is a diffusion layer. The white layer with an average thickness 6.3 µm was created at the plasma nitriding temperature of 500 °C and nitriding period of 10 hours (Fig. 2). It is optically

recognizable on the sample surface. In this case, the diffusion layer is not optically distinct from the core of the material.

3.1 Metallographic structure

Tab. 4 was developed from the measurement results, where thicknesses of particular diffusion layers of steels are documented. In Tab. 4 the values of thicknesses of white layers are also displayed on particular samples. From the table it is obvious that the results are the same for thickness of nitriding layer as well as for the white layer. In sample 5, a minimum increase of diffusion layer is visible, which shows no significant change in subsequent measurements. We can note that all samples had passed through plasma nitriding process at the same conditions and a risen diffusion layer is the same on all samples.

Tab. 4 The results of thickness diffusion and white layers

Sample	Thickness of diffusion layer[mm]	Thickness of white layer [mm]
4	0.38	6.3
5	0.37	6.1
6	0.38	6.5

Source: authors.

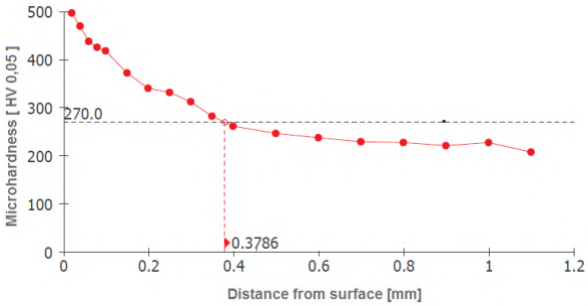

Fig. 3 Micro hardness depth profile sample No. 4
Source: authors.

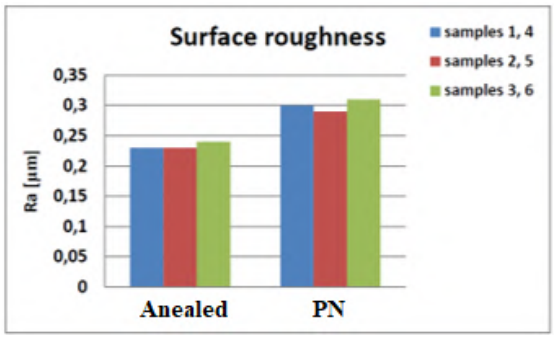

Fig. 4 Surface roughness 1.2842 before (annealed) and after (PN)
Source: authors.

3.2 Surface roughness

Qualitative data on roughness is shown in (Fig. 4). Surface roughness on all samples that have passed through the plasma nitriding process, are deteriorated in average by 30 %, comparing with samples without plasma nitriding. This deterioration was caused by a dedusting process and due to a rise of a new nitride surface layer (Fig. 5 and Fig. 6).

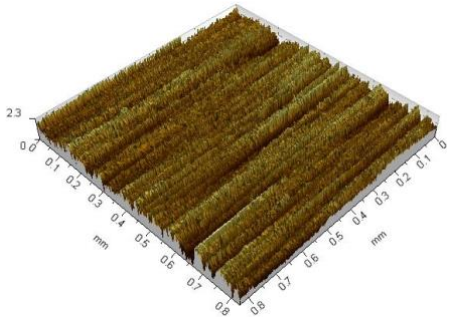

Fig. 5 3D profile steel 1.2842 without application of plasma nitriding; Sa 0.23µm
Source: authors.

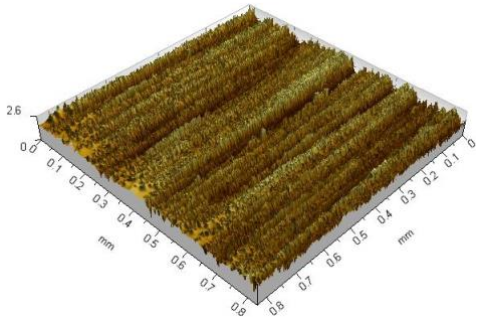

Fig. 6 3D profile of the steel 1.2842 nitrided at 500 °C and time of 10 hours; Sa 0.30 µm
Source: authors.

3.3 Surface wear

The wear shown in the picture 7a), points at a high rate of wear, as this sample had passed only through a basic type of thermal treatment. For the next samples 7b), 8c), 8d), a significant improvement of the surface profile occurred. These samples were plasma nitrided and they featured a much higher

quality of surface. The comparison can be seen in Graph.2 (Fig. 9) between all the measurements of wear at different load parameters and different radiuses of rotation.

The depth of wear was measured with profile meter and the results are displayed on a plot in Graph.3 (Fig. 10). Each measurement of depth was taken on four different places. Subsequently, an average depth of an imprint was defined. The results expressly point at excellent mechanical features of plasma nitrided samples, as their depth of the imprint was ranging only in several micrometers comparing with tempered samples [13, 14].

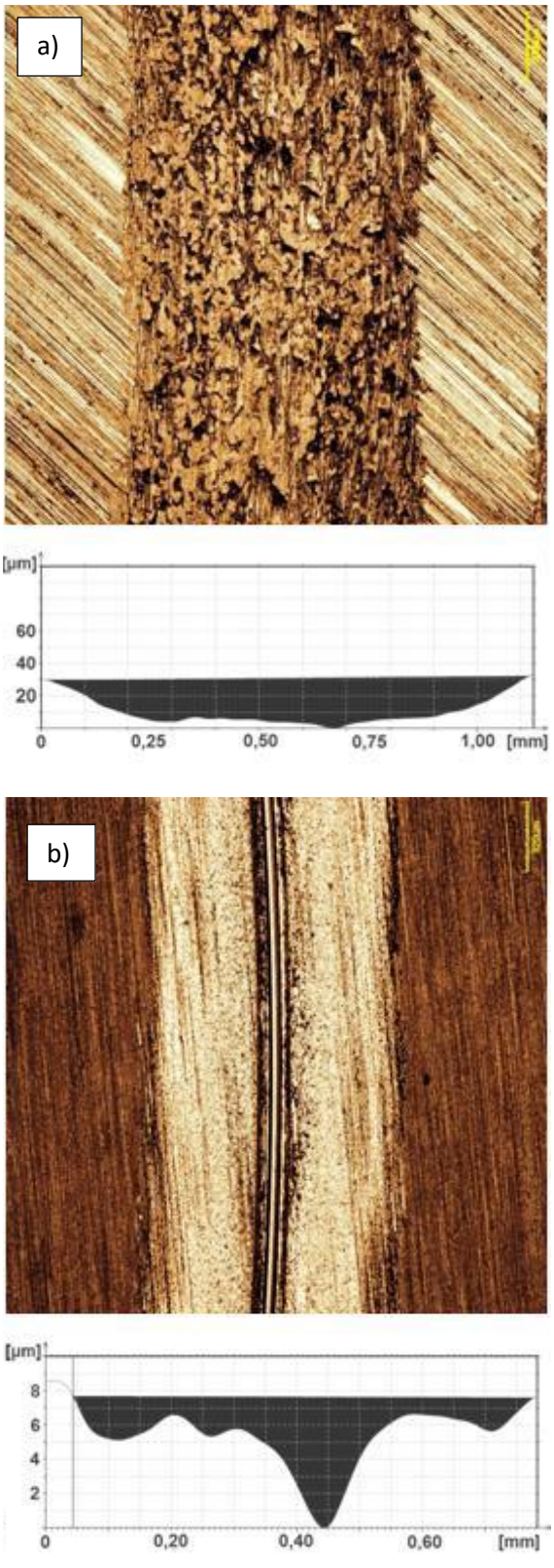

Fig. 7 Surface profiles of wear and depth tracks: a) before PN, COF 0.59 µm, h 31 µm, b) after PN, COF 0.42 µm, h 7.2 µm
Source: authors.

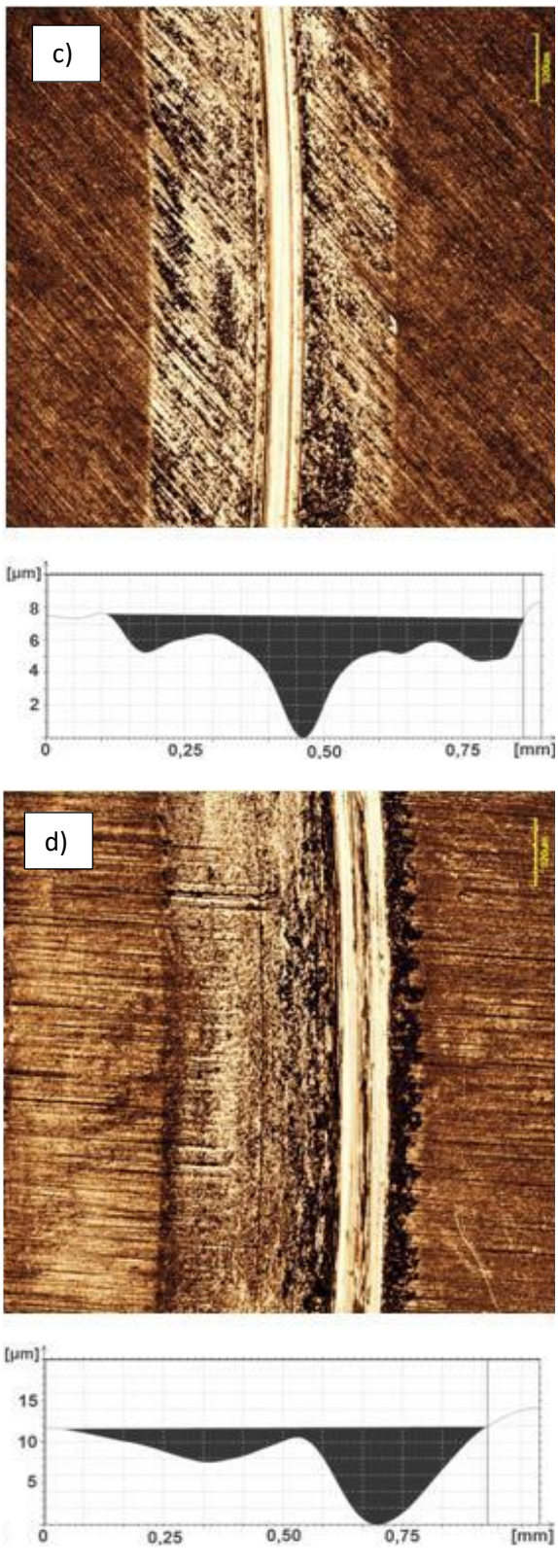

Fig. 8 Surface profiles of wear and depth tracks after PN: c) COF 0.40 µm, h 7.6 µm, d) COF 0.39 µm, h 10.1 µm
Source: authors.

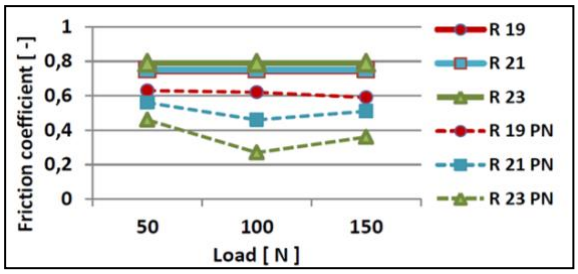

Fig. 9 Comparison of friction coefficient for all samples
Source: authors.

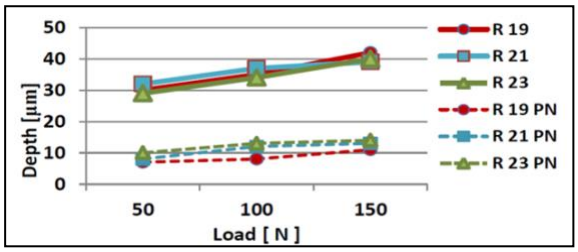

Fig. 10 Comparison indention depth in all samples
Source: authors.

4 CONCLUSION

All measurements were focused on a study of the 1.2842 structural nitride steel. Plasma nitriding was carried out at standard conditions and parameters were chosen in such a way to achieve the best possible diffusion layer. The research brought us some valuable information about mechanical features of the 1.2842 steel. From a study of microstructure and based on the results, the following conclusions can be made:

- The 1.2842 tool steel is suitable for a plasma nitriding process due to its chemical composition and the results of micro structure point at a rise of the diffusion layer of 0.38 µm thickness, mainly composed of ε- phase (Fe_2-3N).
- A surface hardness of tempered samples had a value of 270 HV, it increased after plasma nitriding on average to a value of 500 HV, i.e. We can note, that plasma nitriding significantly increases surface hardness and the lifetime, as well as the majority of degradation processes start spreading from the surface into the material core.
- Material roughness before nitriding process was ranging on the level of 0.23 µm, after plasma nitriding the sur-face quality decreased by 30 % to the value of 0.30 µm. Such deterioration is caused by a dedusting process, when the nitride cations bombard a material surface and subsequently atoms of various elements being on a material surface are shot out.
- Resistance to wear plays one of the most important roles in the material lifecycle. Plasma nitriding process significantly decreases friction coefficient. The friction coefficient decreased at plasma nitrided samples com-paring with samples that had passed only a basic thermal treatment in all three loads. The same results are obtained from an imprint depth, left by a measuring ball. These findings are connected with a rise of a hard diffusion layer on a surface after plasma nitriding process.

From the results of the experiment, we can state that the plasma nitriding improves a quality of mechanical features of the 1.2842 steel except of material roughness. It brings a great benefit in area of improvement of tribological features of materials as well as their application in various sectors of mechanical engineering industry and cutting tools.

References

[1] STUDENÝ, Z., D. DOBROCKÝ and Z. POKORNÝ. Importance of diffusion process on the fatigue life of steel. In: *Manufacturing Technology*. 2017, **17**(1), p. 94–99. Available at: https://doi.org/10.21062/ujep/x.2017/a/1213-2489/MT/17/1/94.

[2] PILCH, O., P. FALTEJSEK, V. HRUBÝ and M. KRBAŤA. The corrosion resistance of turbocharger stator after plasma nitriding process. In: *Manufacturing Technology*. 2017, **17**(3), p. 360–364. Available at: https://doi.org/10.21062/ujep/x.2017/a/1213-2489/MT/17/3/360.

[3] DOAN, T. V., D. KUSMIČ, M. POSPÍCHAL and D. DOBROCKÝ. Improvement of wear resistance for C45 steel using plasma nitriding, nitrocarburizing and nitriding/ manganese phosphating duplex treatment. In: *IOP Conference Series: Materials Science and Engineering*. 2017, **179** (1), p. 1–8. Available at: https://doi.org/10.1088/1757-899X/179/1/012017.

[4] KUSMIČ, D., T. V. DOAN, O. PILCH and M. KRBAŤA. Corrosion resistance and tribological properties of plasma nitrided and tenifered 42CrMo4 steel. In: *METAL 2016 - 25th Anniversary International Conference on Metallurgy and Materials, Conference Proceedings*. 2016, p. 1103-1108.

[5] ULUTAN, M., K. KILIÇAY, E. KAYA and I. BAYAR. Plasma transferred arc surface modification of atmospheric plasma sprayed ceramic coatings. In: *Journal of Mechanical Science and Technology*. 2016, **30**(8), p. 3813–3818. ISSN 1738-494X. Available at: https://doi.org/10.1007/s12206-016-0744-y.

[6] POKORNÝ, Z., V. HRUBÝ and Z. STUDENÝ. Effect of nitrogen on surface morphology of layers. In: *Metallic materials*, 2016, **54**(2), p. 119-124. Available at: https://doi.org/10.4149/km_2016_2_19.

[7] DUBOVSKÁ, R. and J. MAJERÍK. The research analysis of surface finish and wear on the special tribological device. In:, *Procedia Engineering.* 2015, Vol. 100, p. 730–736. ISSN 1877-7058. Available at: https://doi.org/10.1016/j.proeng.2015.01.426.

[8] LANDEK, D., B. LISCIC, T. FILETIN, T. LUBBEN, and D. LISJAK. Hardenability testing and simulation of gas-quenched steel. In: *Materials and Manufacturing Processes*. 2009, **24**(7-8), p. 868–872. ISSN 1042-6914. Available at: https://doi.org/10.1080/10426910902917462.

[9] EKINOVIČ, S., S. DOLINŠEK and E. BEGOVIČ. Machinability of 90MnCrV8 steel during high-speed machining. In: *Journal of Materials Processing Technology*. 2005, **163**(1-3), p. 603–608. ISSN 0924-0136. Available at: https://doi.org/10.1016/j.jmatprotec.2005.02.178.

[10] AXÉN, N. and K. H. ZUM GAHR. Abrasive wear of TiC-steel composite clad layers on tool steel. In: *Wear*. 1992, **157**(1), p. 189–201. ISSN 0043-1648. Available at: https://doi.org/10.1016/0043-1648(92)90197-G.

[11] TAYLAN, F., O. ÇOLAK and M. C. KAYACAN. Investigation of TiN Coated CBN and CBN cutting tool performance in hard milling application. In: *Strojniski Vestnik/Journal of Mechanical Engineering*. 2011, **57**(5), p. 417–424. ISSN 0039-2480. Available at: https://doi.org/10.5545/sv-jme.2010.059.

[12] BARRENA, M. J., J. M. GÓMEZ DE SALAZAR and L. MATESANZ. Interfacial microstructure and mechanical strength of WC-Co/90MnCrV8cold work tool steel diffusion bonded joint with Cu/Ni electroplated interlayer. In: *Materials and Design*. 2010, **31**(7), p. 3389–3394. ISSN 0261-3069. Available at: https://doi.org/10.1016/j.matdes.2010.01.050.

[13] KRBAŤA, M., M. ECKERT, J. MAJERÍK and BARENYI, I.: Wear behaviour of high strength tool steel 90mncrv8 in contact with Si3N4. In: *Metals* [online]. 2020, No 756, p. 1–17. Available at: https://doi.org/10.3390/met10060756.

[14] KRBAŤA, M., M. ECKERT, L., BARTOSOVA, I. BARENYI, J., MAJERÍK, P. MIKUŠ and P. RENDKOVA. Dry sliding friction of tool steels and their comparison of wear in contact with ZrO2 and X46Cr13. In: *Materials,* 2020, **13**(10), p. 1–21. ISSN 1996-1944. Available at: https://doi.org/10.3390/ma13102359.

Dipl. Eng. Michal **KRBAŤA**, PhD.
Department of Engineering Technologies and Materials
Faculty of Special Technology
Alexander Dubček University of Trenčín
Ku kyselke 469
911 06 Trenčín
Slovak Republic
E-mail: michal.krbata@tnuni.sk

Dipl. Eng. Jana **ESCHEROVÁ**
Department of Engineering Technologies and Materials
Faculty of Special Technology
Alexander Dubček University of Trenčín
Ku kyselke 469
911 06 Trenčín
Slovak Republic
E-mail: jana.escherova@tnuni.sk

Michal Krbaťa – was born in Trenčín, Slovakia in 1988. He received his engineering and PhD. degrees at Alexander Dubček University of Trenčín, Faculty of Special Technology in Trenčín. In his research he focuses on materials research, tribology and dilatometry.

Jana Escherová – was born in Banovce nad Bebravou, Slovakia in 1995. She received engineering degree at Alexander Dubček University of Trenčín, Faculty of Special Technology in Trenčín. In his research he focuses on materials research and technological research.

SCIENCE & MILITARY - WRITER´S GUIDELINES

1. Scientific articles submitted for publishing have to be original, topical and never been published before.

2. Articles have to be written in English language and in accordance with ethical standards. For more details, please visit the website of the Science & Military Journal (http://sm.aos.sk/index.php/en/for--authors-en/ethical-standards).

3. Length of the article should not exceed 6 pages in defined format. Microsoft Word text editor must be used for writing. Articles must be written using Times New Roman, single line spacing and follow the following form: Title -12 point bold capital letters aligned to the center. Full author´s (co-author´s) name – 10 point normal letters aligned to the center. Abstract – 9 point normal letters, extent 3-5 lines. Keywords – 9 point normal letters. The article text – 10 point normal letters. Contact - full author´s (co-author´s) name, affiliation, e-mail – 9 point normal letters at the end of the article. The article text will be written in 2 columns format with a 75 mm column width and 10 mm empty space separating the columns. The first line of each paragraph must be shifted 5 mm to the right.

4. Upper and lower margins must be set to 25 mm, left and right margins to 20 mm. Select mirror margins and set binding margins to 10 mm. The distance between the header/footer and the page margin must be 12,5 mm, while different odd and even pages must be selected.

5. Photographs for publication must be in black-white (not in color) of excelent quality with good contrast.

6. Equations in the text are also to be written using the equation editor. (Equation must be typed in Microsoft Equation, which is an integral part of Microsoft text editor.) They must be numbered. Numbers are to be enclosed in parentheses and aligned to the right margin of a column.

7. Figures, graphs and tables must be included in the text and numbered and must contain description. Figures must be identified as Fig. 1 followed gradually by the figure description. Graphs must be identified as Graph 1 followed by the graph description. Tables must be identified as Tab. 1, followed by the table description.

8. References must be fully and accurately documented (according to ISO 690). References should be quoted in the text in square brackets and listed in the order they have appear in the text.

9. The specimen article that can be found on the web-site: http://sm.aos.sk/index.php/en/for-authors-en can be used as an example of the correct format.

10. The editorial board will consider submitted articles in the next scheduled meeting. If it decides to include the article in the next issue it submits the manuscript to the editors for the peer review. The final version (before printing) will be sent to the author for the final revision. The authors are fully responsible for the level of language.

11. Contributions in A4 format edited according to the specimen article should be submitted in one hard copy and also in electronic form to the Editorial board.

12. The deadlines for the delivery of the articles in calendar year are: March 1 and September 1.

SCIENCE & MILITARY

No 1 | Volume 16 | 2021

Content

ISSN 1336 – 8885 (print)
ISSN 2453 – 7632 (on-line)